# Benefits of double $\alpha$ coincidence analysis of $^{12}$C

-Yielding twice the quantity of data, with only twice the work

Villads Lundsteen Jacobsen

Student number: 201608922

Department of Physics and Astronomy, Aarhus University

Supervisor: Karsten Riisager

August 29, 2023

# Contents

**Abstract**

This thesis presents an extended analysis of the $\beta$-delayed triple $\alpha$ decay of $^{12}$N from [1]. The analysis consists of: Reproducing key spectra from earlier work, estimating geometrical effects with *Geant4* simulations, evaluating the benefits of double $\alpha$ coincidence analysis and $\alpha$-$\beta$ angular studies for determining the presence of forbidden decays. The double $\alpha$ coincidence analysis yielded around twice the quantity of data for events that resemble uniform phase space distributed decays and for $^{8}$Be ground state decays of $^{12}$C excitation energies around $600 - 2000$keV. The *Geant4* simulations revealed the presence of systematic errors from our detector setup and beam profile. The size of these errors changed the outcome of the $\alpha$-$\beta$ study to a degree in which the presence of forbidden decays could not be concluded.

# 1 Introduction

Studying the structure of the $^{12}$C nucleus has been ongoing for approximately 60 years. This field has its main motivation from stellar fusion models and has since spiked many interesting debates of scattering experiments in contrast to decay experiments. In this chapter, we will discuss the earlier research performed, as well as how this master thesis can contribute to the field. The studies of $^{12}$C often have a very similar introduction section structure including history, theoretical models, recent studies, and an outline. This introduction chapter is inspired by the earlier work on the experiment studied in this work [1], and Andreas Gads' Ph.D [2].

## 1.1 Brief history of $^{12}$C

### Stellar fusion models

*Where do we come from?* A question that can fit many perspectives. For a biologist, it might refer to the theory of evolution. To a psychologist, it might spark a debate about the consciousness of humans in contrast to animals. But to a physicist, it refers to the creation of the very matter we consist of. We know today that the matter our planet consists of most likely was produced in stellar fusion processes [3]. Here the main fusion process for the early life of a star is the fusion of hydrogen to helium. A long range of different fusion processes and neutron capture followed by *beta*-decay allows for a very good under-

standing of element creation in stars. These models can very easily be tested by examining our planet/universe. Do we find the same ratios of elements on earth as predicted by these stellar models? When these models were first proposed, the answer was no. There was an abundance of a variety of elements e.g. carbon. Since carbon is such a vital part of life on earth, this was quite an issue. Originally the production of carbon was believed to occur when an $\alpha$ particle fused with $^8$Be (two $\alpha$ particles). The fusion of two $\alpha$ particles to $^8$Be is very unstable, and quickly disperses (half-life of $10^{-17}$s) if not a third $\alpha$ intercepts to create $^{12}$C. But even then, the excited state of $^{12}$C created in these hot and dense environments will quickly decay into three $\alpha$ particles again, leaving us where we started. This is referred to as the triple-$\alpha$ process. It was then suggested by Salpeter and Öpic ([4], [5]), that if $^{12}$C could live long enough to de-excite to a stable state through the triple-$\alpha$ process $^8\mathrm{Be}(\alpha,\gamma)^{12}\mathrm{C}$, then $^{12}$C could be produced. Is this enough to explain the abundance of carbon? Unfortunately not. To solve this we must introduce Fred Hoyle. For further studies of the Hoyle state history we refer to an article written by Helge Kragh [6].

## The Hoyle state

Fred Hoyle was the person to improve the understanding of the triple-$\alpha$ process and explain the carbon abundance in the universe. He showed that only if the $\alpha$ particle is captured in $^8$Be resonantly through an unobserved state (now known as the Hoyle state), then the abundance of carbon could be explained [7]. The state was verified in a $^{14}\mathrm{N}(d,\alpha)^{12}\mathrm{C}$

experiment to have the energy and width of $E = 7.68(3)$MeV above the ground state and $\Gamma < 25$keV [8], which is almost exactly what Hoyle predicted. Later experiments [9] evaluated the spin and parity of the state to be $J^\pi = 0^+$, in a $\beta$ decay experiment. The carbon abundance in the universe was explained by the triple-$\alpha$ process with the inclusion of the Hoyle state. This result made some very successful stellar nuclear models possible and made an example of great collaboration between astro and nuclear physics. Nuclear states above the Hoyle state became interesting, and strange broad resonances were observed.

## Broad resonances and ghosts

By measuring the $\alpha$ particle from $^{12}$B $\beta$-decay, broad resonances at a peak value of 10.1 MeV and a FWHM of 2.5 MeV was found [10]. The selection rules (See equation (2.2)) for $\beta$-decay restricted this to be $0^+$ or $2^+$ states. To complicate matters more Barker and Treacy [11] showed that an isolated state near a particle threshold (like the triple $\alpha$ threshold in $^{12}$C) gives rise to a satellite peak, above the "real" peak. This is referred to as the *ghost* peak. It was predicted that the ghost peak of the Hoyle state would be located in same area as the potential $0^+/2^+$ state. However the ghost peak could not account for the whole broad peak, so two broad resonances at 10 MeV and 11.8 MeV was proposed. This is how the research and the interest in $^{12}$C structure above the Hoyle state started. The newest data of the lower energy levels can be found in table 1.1. While much more can be said

about interesting work on $^{12}$C ($\alpha$ clustering, disagreement between decay and scattering experiment etc.) this is enough to understand the potential struggles of the earlier work and hence the motivation for this thesis. More elaborate background knowledge of the $^{12}$C studies can be found in [1] and [2].

| Energy [MeV] | $\Gamma$ [keV] | $J^\pi$ |
|---|---|---|
| g.s | - | $0^+$ |
| 4.43982(21) | 10.8(6) $\times 10^{-6}$ | $2^+$ |
| 7.65407(19) | 9.3(9) $\times 10^{-3}$ | $0^+$ |
| 9.641(5) | 46(3) | $3^-$ |
| 9.870(60) | 850(85) | $2^+$ |
| (9.930(30)) | 2710(80) | $0^+$ |
| (10.3(3)) | 3000(700) | $(0^+)$ |
| 10.847(4) | 273(5) | $1^-$ |
| 11.836(4) | 230(8) | $2^-$ |
| (12.4) | broad | $(5^+\ 4^-\ 6^-\ 7^+)$ |
| 12.710(6) | 18.1(28) | $1^+$ |
| (13.3(2)) | 1700(200) | $4^+$ |
| 13.316(20) | 360(43) | $4^-$ |
| 14.079(5) | 272(6) | $4^+$ |
| 15.110(3) | 45.6(10) $\times 10^{-3}$ | $1^+$ |
| 15.44(40) | 1770(200) | $(2^+)$ |

**Table 1.1:** *Low energy levels of $^{12}C$ from [12]. The values in parenthesis are tentative.*

## 1.2 Earlier studies and outline.

The work in this master's thesis is based on an experiment from 2014 performed by Jonas Refsgaard [1]. This decay experiment sought out to study a wide energy range of the $^{12}$C spectrum and produce R-matrix fit [13] to the different decay types in the said spectrum. Studying the underlining resonances in the broad peak around 9-13 MeV, but also the higher-lying structures above 12.7 MeV (See table 1.1). A general struggle in decay experiments is that we often have many near lying states (or ghost peaks), creating "noise" in areas of interest, while in other areas there are too few data points. Also, our detector setup can limit us to have a low acceptance of certain decays. In this work, we will try to improve on the analysis performed by Jonas Refsgaard (and other people who have studied $^{12}$C with decay experiments) by examining the potential of double $\alpha$ coincidence analysis. That is to say, instead of detecting three $\alpha$ particles, we only look at events where two are detected and reconstruct the third $\alpha$ from conservation of momentum. We will investigate the acceptance of different decay types for the double and triple $\alpha$ coincidence analysis method, and thereby find under which circumstances such an analysis can be beneficial. We will also try to replicate many of the original results and expand upon the simulation method used in [1]. Furthermore, a later study (2017) was performed with the same experimental setup as in [1], in which strong signals of first forbidden $1^-$ and second forbidden $2^+$ decays from $^{12}$C was observed [14]. These signals were determined from $\alpha$-$\beta$ angular analysis. An attempt to replicate these results from

the [1] data set is performed as well.

It should be noted that all this will be elaborated upon in the chapters to come.

# 2 Theory

The theory described in this work is largely inspired by the original work on this experiment [1]. The topics to cover are: understanding the $\beta$-decay of $^{12}$N, how to analyse the data through the sequential decay model and presenting these results in Dalitz plots. Furthermore, we will elucidate under which circumstances an angular correlation between the $\beta$ and highest energy $\alpha$ can arise.

## 2.1 $\beta$-Decay of $^{12}$N

The reaction of interest for this experiment is the following decay chain:

$$^{12}\mathrm{N} \longrightarrow^{12} \mathrm{C} + \beta + \nu \longrightarrow^{8} \mathrm{Be} + \alpha \longrightarrow \alpha + \alpha + \alpha \tag{2.1}$$

With a half-life of 11 ms [15] the radioactive isotope $^{12}$N undergoes $\beta$ decay into $^{12}$C which can decay to $^{8}$Be with $\alpha$ decay. From this decay chain many possible decay channels can contribute with decays through different excitation states in $^{12}$C and $^{8}$Be. A level scheme of possible decay channels is shown in figure 2.1.

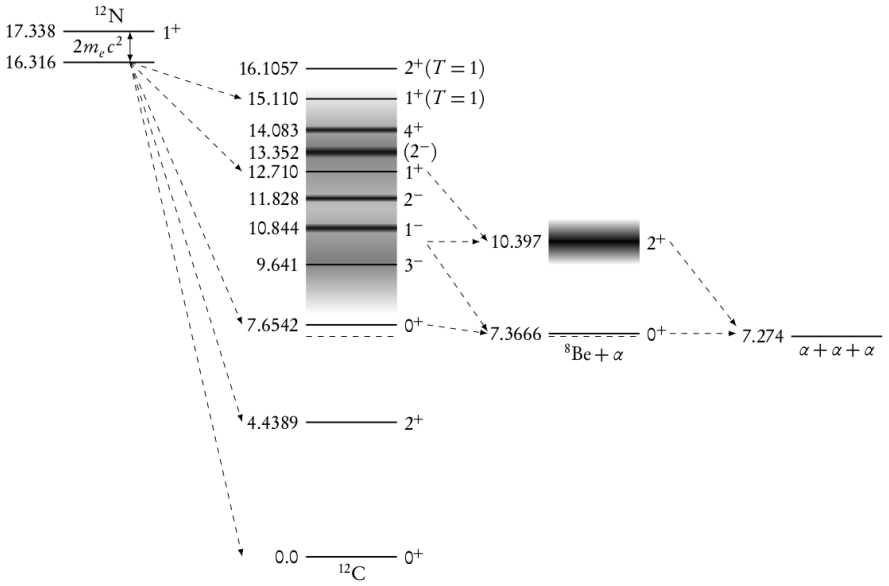


**Figure 2.1:** *Level diagram of the $\beta$-delayed triple-$\alpha$ decay from $^{12}$N. Here numbers on the left side indicate the energy of the state relative to the ground state $^{12}$C in units of MeV. The numbers on the right side of a state is spin and parity, $J^\pi$. The allowed transitions indicated by the dashed arrows are described in the text.*

From figure 2.1 we can see the relevant nuclear states and possible decay paths indicated by the dashed arrows. Why only certain decays are allowed follows from the fact that beta decays are an instance of the weak interaction. By examining the weak interaction Hamiltonian in the non-relativistic limit, you find a set of selections rules that dictates the leading order behaviour of beta decays [16]. These selection rules lead to a restriction on the coupling of the angular momenta of the lepton pair (electron/positron and neutrino/anti-neutrino). This

allows for two types of transitions to occur. *Fermi-transitions* are when the lepton pair have anti-parallel spin **S** and hence the angular momentum of the initial and final states are unchanged $\Delta\mathbf{J} = 0$, since $\mathbf{J} = \mathbf{L} + \mathbf{S}$ where **L** is the orbital angular momentum which is 0 for allowed transitions. *Gamow-Teller transitions* are when the spins of the lepton pair is parallel, giving rise to $\Delta\mathbf{J} = 0, \pm 1$. These transitions can be written shortly as:

$$\begin{aligned} \mathbf{S}_e + \mathbf{S}_\nu = 0 &\longrightarrow \Delta\mathbf{J} = 0 \\ \mathbf{S}_e + \mathbf{S}_\nu = 1 &\longrightarrow \Delta\mathbf{J} = 0, \pm 1 \end{aligned} \tag{2.2}$$

For allowed transitions ($\mathbf{L} = 0$) parity, $\pi$, is conserved ($\pi = (-1)^l = 0$). Hence decays from the ground state $\mathrm{J}^\pi = 1^+$ in $^{12}$N, only allows for transitions to $0^+$, $1^+$ and $2^+$. Another restriction we have concerns the energy of the decays. The Q value of the $^{12}$N $\beta$-decay is:

$$Q = (M_{^{12}\mathrm{N}} - M_{^{12}\mathrm{C}} - 2M_e)c^2 = 16.316 \text{ MeV} \tag{2.3}$$

This implies that only states with excitation energy below 16.316 MeV can be populated in the decays. From restrictions in the energy, we have 11 possible decay options, in which only 5 (including the ground state of $^{12}$C) are eligible based on the selection rules from equations (2.2). These are the decays drawn in figure 2.1. To be able to decay further from $^{12}$C to the $^8$Be the excitation energy of $^{12}$C needs to exceed the triple-$\alpha$ energy threshold:

$$(3M_\alpha - M_{^{12}\mathrm{C}})c^2 = \ 7.274\text{MeV} \tag{2.4}$$

Excitation energies above this threshold allow for at least two types of decays. Namely, $\gamma$ and $\alpha$ decays. For the $\alpha$ decay we can write $^{12}\mathrm{C} \longrightarrow {}^{8}\mathrm{Be}* + \alpha$, as written in equation (2.1). Here * marks that the nucleus is in an excited state (as one should be when doing physics). Since $^{8}$Be* is unbound it decays almost immediately into two $\alpha$ particles (half-life of $10^{-17}$ s). This is why this reaction is often referred to as $\beta$-delayed triple-$\alpha$ decay.

## 2.2 Dalitz-plots

To be able to distinguish the different decay possibilities as shown in figure 2.1, we need to present our data in a clever way. Introducing Dalits plots [17]. Dalitz plots are a way to represent the data from reactions with 3 fragments in the final state. Instead of simply plotting the energies of the three $\alpha$ particles $E_1$, $E_2$ and $E_3$ (where $E_1 > E_2 > E_3$), we change our coordinate system. Our new coordinate system is defined in figure 2.2.

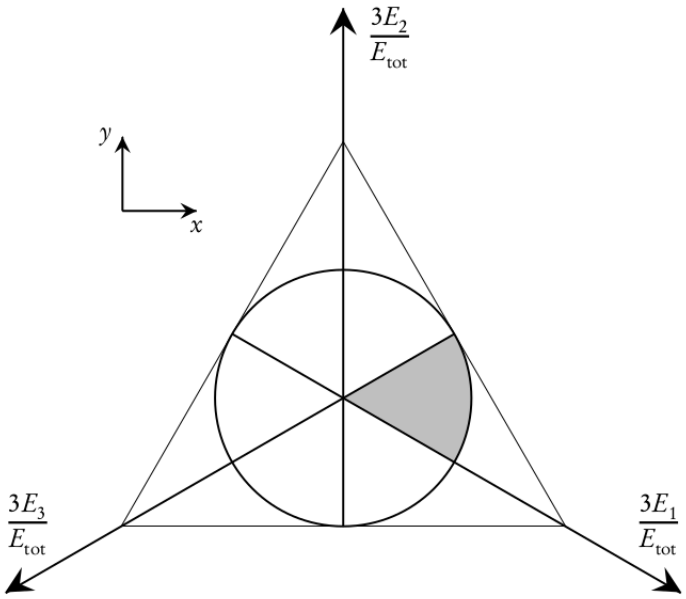


**Figure 2.2:** *Overview of how Dalitz plot coordinates are defined. The kinematics of a three-particle decay can be completely described in this manner. Here $E_1$, $E_2$ and $E_3$ are the energies of the particles in order of decreasing energy, and $E_{tot} = E_1 + E_2 + E_3$. Further description can be found in the text.*

Here $E_{tot} = E_1 + E_2 + E_3$. From conservation of energy, the plot is restricted to the equilateral triangle in the plot. Furthermore from the conservation of momentum and the fact that our three particles are identical, the plot narrows down to within a circle of radius of 1. Since we chose our energies in the order $E_1 > E_2 > E_3$ this further restricts the plot so all the relevant kinematic information is available in the marked grey area of figure 2.2. This is a good way to represent our

data since a decay with a uniform phase space distribution will show a uniform data distribution in our plot. All the interesting physics will then show itself as maximums and minimums in the plot. These facts about the nature of our Dalitz plots and how uniformly phase space decays are represented in them are not trivial. They are merely stated here to make it easier for the reader to follow conclusions and discussions in later sections. To describe our data in this marked area, we make the coordinate transformation:

$$\begin{aligned} x &= \frac{\sqrt{3}(E_1 - E_3)}{E_{tot}} \\ y &= \frac{2E_2 - E_1 - E_3}{E_{tot}} \end{aligned} \tag{2.5}$$

Where the origin is $E_1 = E_2 = E_3$ (centre of the figure 2.2).

## 2.3 The sequential decay model

In this work, we use the sequential decay model to calculate decay amplitudes used for our simulations. In this context, sequential refers to our decay as a two-step process. Step one is the $\alpha$-decay from $^{12}$C to $^{8}$Be, and step two is the $^{8}$Be breakup into two $\alpha$ particles. The breakup amplitude from such a model has been found in [18] and [19].

$$\begin{aligned} f_{1-23} = \sum_{m_b} \langle l\ m_a - m_b\ j_b\ m_b | j_a\ m_a \rangle\, Y_l^{m_a - m_b}(\Theta_1, \Phi_1) Y_{l'}^{m_b}(\theta_2, \phi_2) \\ \times \frac{\sqrt{\Gamma_1 \Gamma_2 / \sqrt{E_1 E_{23}}} e^{i(\omega_l - \phi_l)} e^{i(\omega_{l'} - \phi_{l'})}}{E_0 - \gamma_2^2 [S_{l'}(E_{23}) - S_{l'}(E_0)] - E_{23} - \frac{i}{2}\Gamma_2} \end{aligned} \tag{2.6}$$

There is quite a bit to cover with the indexing of this monstrosity of an equation. Down below is an overview of the different symbols in equation (2.6) in list format.

- $j_a$ Spin of decaying state in $^{12}$C.
- $j_b$ Spin of $^8$B resonance.
- l Orbital angular momentum in $^{12}\text{C} \rightarrow ^8\text{Be} + \alpha$.
- l' Orbital angular momentum in $^8\text{Be} \rightarrow \alpha + \alpha$.
- $\Gamma_1$ Partial width of $^{12}\text{C} \rightarrow ^8\text{Be} + \alpha$ channel.
- $\Gamma_2$ Partial width of $^8\text{Be} \rightarrow \alpha + \alpha$ channel.
- $E_1$ Kinetic energy of $\alpha_1$ in $^{12}$C rest frame.
- $E_{23}$ Relative kinetic energy of $\alpha_2$ and $\alpha_3$.
- $E_0$ Energy of the intermediate state in $^8$Be measured from the two-$\alpha$ threshold.
- $\omega_l$ Coulomb phase shift.
- $\phi_l$ Hard sphere phase shift.
- $S_{l'}$ R-matrix shift function.
- $\Omega_1, \Theta_1$ Direction of emission of $\alpha_1$ in the $^{12}$C rest frame
- $\omega_2, \theta_2$ Direction of emission of $\alpha_2$ in the $^8$Be rest frame.
- $m_b$ is the magnetic quantum number of $^8$Be
- $m_a$ is the magnetic quantum number of $^{12}$C

In equation 2.6, the subscript $1-23$ indicates the order of emission. The two-step process mentioned above. Since we can not determine in our measurements which $\alpha$ particle was emitted first, we need to

average out the amplitude in order of emission:

$$|f|^2 = \sum_{m_a} |f_{1-23} + f_{2-31} + f_{3-12}|^2 \tag{2.7}$$

Up till this point, the sequential treatment of the decay chain has not been introduced to the problem. Inspired by an interesting argument as presented in [1], we will look at the distance between the first $\alpha_1$ emitted and the $^8$Be recoil when the second breakup begins. The validity of treating each breakup separately can be checked by calculating the expected Coulomb interaction. The range is calculated from the velocity of $\alpha_1$, $v = \sqrt{2\epsilon_1/\mu}$ and the lifetime of the nuclear state of $^8$Be. Where $\mu$ is the reduced mass (In the CM system) and $\epsilon_1$ is the energy released in the $^{12}$C break up. As an example, consider the decays from the $1^+$ excited state in $^{12}$C. According to the selection rules 2.2, the only open decay channel is to the $2^+$ state in $^8$Be. The Lifetime of $2^+$ state in $^8$Be is calculated as $\tau = \hbar/\Gamma_{obs}$, where $\Gamma_{obs}$ is the observed reduced decay width of the $2^+$ state from [20]. From this calculation, we obtain:

$$(v\tau)_{2^+} \approx 5.1 \text{ fm} \tag{2.8}$$

We assume that the distance between $\alpha_1$ and Be from the first break up is given by the channel radius, which is around 5 fm. The channel radius, $a$, is a measure from R-matrix theory for the boundary between the regime of the strong- and the Coulomb forces. For distances $r$, where $a < r$, the system interaction is dominated by the Coulomb force, whereas for $a > r$ the system mainly interacts through the strong force. We calculate a total distance of 10 fm. This is however not

satisfactory, since at these distances the Coulomb energy between the $^8$Be and $\alpha$ is around 1.1 MeV. Which is similar to the kinetic energy of $\alpha_2$ and $\alpha_3$. To correct for this effect, equation (2.6) have been modified to account for this Coulomb effect. The correction is included in the calculation of the penetrability which is used to calculate the reduced width $\Gamma = 2P_l\gamma$ in equation (2.6). The penetrability is a function of energy and describes how likely it is for a particle to penetrate the potential barrier of the nucleus. So in this case it is the likelihood of an $\alpha$ particles escaping the potential barrier of $^{12}$C or $^8$Be.

## 2.4 Expected transitions

To be able to interpret the Dalitz plots, we must first understand how different nuclear transitions appear in such figures. This has already been done in earlier works [1], and the results are plotted in figure 2.3 and 2.4. Here each row represents a nuclear transition at four different $E_{tot}$ values. Namely, 1 MeV, 3 MeV, 5 MeV and 7 MeV. Each transition is labelled with the three indexes $j_a$, $l$ and $j_b$. A brief description is in place: $j_a$ is the spin of the $^{12}$C nuclear state, $l$ is the orbital angular momentum of the $^8\text{Be} + \alpha$ system and $j_b$ is the spin of the $^8$Be unbound nuclear state. All the allowed transitions are also shown in table 2.1.

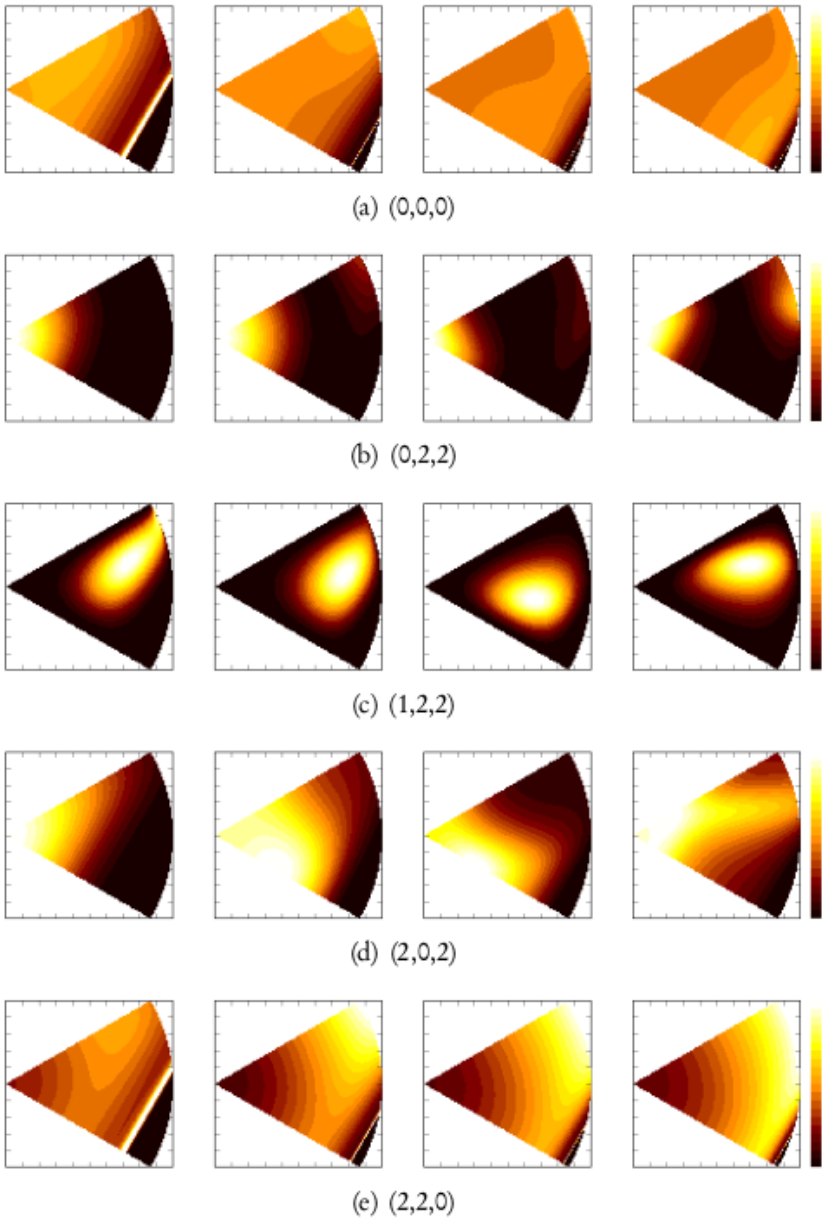




**Figure 2.3:** *See description in figure 2.4.*

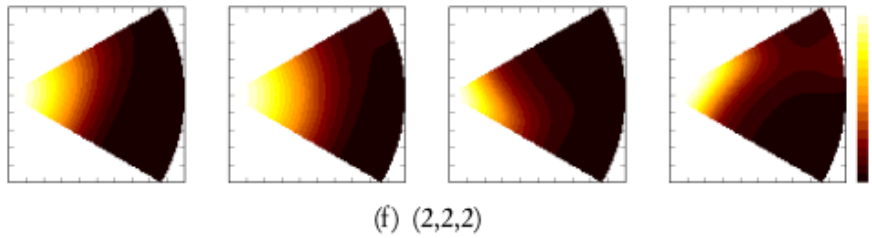

(f) (2,2,2)

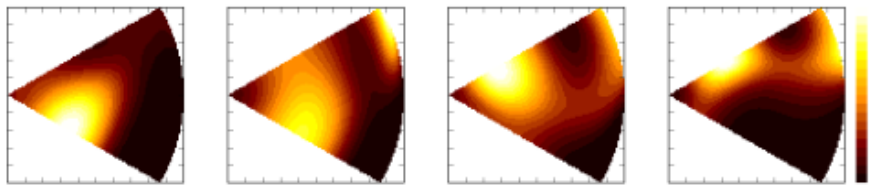

(g) (2,4,2)

**Figure 2.4:** *Expected Dalitz plot for different nuclear transitions of* (2.1)*, with indices* $j_a$*,* $l$ *and* $j_b$*(described in text). Here each row is one decay mode for four total energies,* 1 MeV*,* 3 MeV*,* 5 MeV *and* 7 MeV *(plotted from left to right). The color scale is linear in density. The plots are taken from [1].*

| | | | | | | | |
|---|---|---|---|---|---|---|---|
| $j_a$ | 0 | 0 | 1 | 2 | 2 | 2 | 2 |
| $l$ | 0 | 2 | 2 | 0 | 2 | 2 | 4 |
| $j_b$ | 0 | 2 | 2 | 2 | 0 | 2 | 2 |

**Table 2.1:** *Allowed decay modes for* (2.1)*, calculated from the selection rules in* (2.2)*.* $j_a$ *is the spin of the* $^{12}C$ *nuclear state,* $l$ *is the orbital angular momentum of the* $^8$Be $+$ $\alpha$ *system and* $j_b$ *is the spin of the* $^8$Be *unbound nuclear state.*

## 2.5 $\beta$-$\alpha$ angle correlation

One of the motivations for this thesis was to study angular correlations between the most energetic $\alpha$ particle, $\alpha_1$, from the $^{12}$C $\alpha$-decay and the $\beta$ from the $^{12}$N $\beta$-decay. You might ask *"Well why should there be any angular correlation, to begin with?"* Good question! It turns out the angular correlation only has a significant contribution from the first forbidden and second forbidden transitions. First, we examine allowed transitions. We look at the angular distribution of an $\alpha$-decay from a polarized nucleus. Here we mean polarised in terms of the magnetic sub-state of the nuclei in the initial state $m_i$ final state $m_f$. The quantum number, $m_{i,f}$ is the projection of the spin on the momentum vector of the decaying particle (in this case the $^{12}$C). An expression for such an $\alpha$-decay can be found in [14].

$$W(\theta) = \sum_{m_i} p(m_i) G(m_i, m_f) W(\theta)_{m_i \to m_f} \tag{2.9}$$

where $W(\theta)_{m_i \to m_f}$ is the directional distribution function for initial spin projection $m_i$ to a final state spin projection $m_f$. $G(m_i, m_f)$ is the relative transition probability between the two states. $p(m_i)$ is the probability of decaying to a $m_i$ state from the $^{12}$N $\beta$-decay. A very long and tedious expression for $p(m_i)$ can be found in Siegbahn K. *Alpha-, Beta-, and Gamma-ray Spectroscopy* [21]. Here, we merely note that the $p(m_i)$ values for allowed transitions (l=0) gives rise to an isotropic angular distribution in equation 2.9. However, when we use a more general expression for $W(\theta)$(from Morita M. [22]) a non-isotropic contribution arises. This contribution can be simplified and

written as:

$$W(\theta) = 1 - A_2 \, P_2(\cos\theta) \tag{2.10}$$

where $P_2(\cos\theta)$ is the second-order Legendre polynomial, and $A_2$ is the anisotropy factor that have contributions from $^{12}$C $\alpha$ decay and $^{12}$N $\beta$ decay. This is expressed as $A_2 = A_{2\alpha} \cdot A_{2\beta}$, where $A_{2\alpha}$ can be calculated with [14, equation (3.10)] and is fixed. $A_{2\beta}$ only has contributions from higher order matrix element from the $\beta$-decay. It has the subscript 2 (referring to $2^+$ state), since we know $0^+$ is always isotropic. The only non-isotropic contribution can arise from the $2^+$ state or potentially $1-$ state. It is important to note that transitions from $2^+$ in $^{12}$C to $0^+/2^+$ in $^8$Be can occur through an allowed or second forbidden transition. Where of course the first one is much more likely. Second forbidden decays should (at best) only account for $1-2\%$ of the decays (referring to fig 24.4 in [23]). Therefore it is highly unlikely that we should measure any significant contributions from these decays. However, new research [14], have found exactly such a contribution. They found the second forbidden transition from $2^+$, to have an anisotropy two order of magnitudes larger than the calculated values from [24].

# 3 Experiment

The work presented in this thesis is based on the experiment performed at the *University of Jyväskylä* in Finland in 2014. Here the radioactive beam facility, IGISOL, was used to study the $\beta$-delayed $\alpha$ decay of $^{12}$C.

The $^{12}$C-ions are produced through $\beta+$ decay from $^{12}$N-ions. The experiment goes as follows: $^{12}$N-ions are produced through a transfer reaction and sent into a carbon foil with an energy of 29.9(1) keV. The foil thickness is chosen to be roughly 110 nm to ensure a complete stop of the $^{12}$N-ions. More on the exact determination of the foil thickness in section *4.5*. The foil is surrounded by double-sided silicon strip detectors (DSSSD) which have a solid-angle coverage of $\approx 49\%$ out of $4\pi$. The rather large solid-angle coverage is to ensure a good triple-$\alpha$ coincidence detection efficiency. It is important to note that since I did not participate in this experiment, most of this chapter will be based on the description of the previous work [1].

## 3.1 IGISOL in Jyväskylä

IGISOL stands for *Ion-Guide Isotope Separation On-Line* and is a facility that exceeds in producing low energy ion beams. The name is rather descriptive of its function since it is a technique that separates the desired ion while it is being transported through an ion-guide. A visualization of the technique is shown in figure 3.1. The process starts with a 30 MeV proton beam that hits a primary target made of natural Carbon. A range of different isotopes is produced and recoiled off of the target. One of these is $^{12}$N, which is created via the $^{12}\mathrm{C}(p,n)^{12}\mathrm{N}$ reaction. The isotopes are then transported together with the flow of He gas into the ion-guide. The ion-guide works as a mass spectrometer, and only allows certain isotopes to enter the extraction electrode by

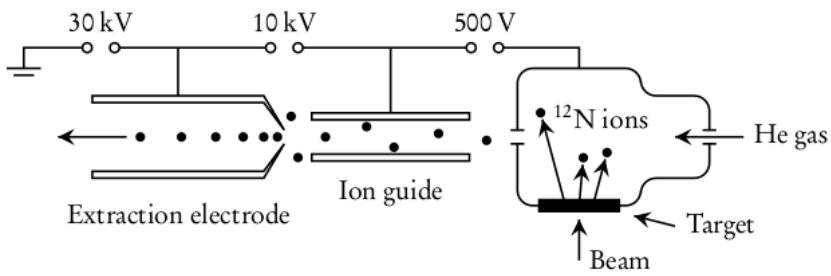


**Figure 3.1:** *Drawing of the technique used at IGISOL [25] to generate low energy ion beams. Note that the voltage written is only an indication of the order of magnitude used in the experiment. The drawing is taken from [1].*

applying a specific voltage in the ion-guide. From then the ions are electrostatically accelerated to the desired experiment. In our case the $^{12}$N ions are accelerated to 29.9(1) keV before they hit our carbon target foil.

## 3.2 Detector setup

The detector setup consists of six double-sided silicon strip detectors (DSSSD) and three silicon pad detectors (PAD). The setup is shown in figure 3.2.

The DSSSD consist of 16x16 strips and have thicknesses as described in table 3.1. Their main purpose is detecting $\alpha$ particles. However, the U3 and U4 detectors are sufficiently thick to detect $\beta$ particles as well. This is needed to study $\beta$-$\alpha$ angular correlations. The DSSSDs are of the W1 type from *Micron Semiconductor Ltd.*

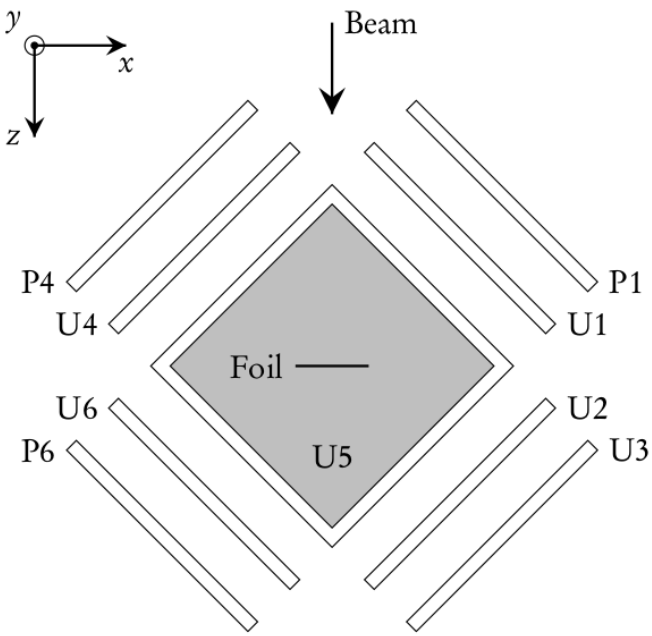


**Figure 3.2:** *Overview of the detector setup. Here the detectors labelled U# is DSSSD and the detectors labelled P# is silicon pad detectors. [1]*

The strips consist of 16 front strips, and 16 back strips orthogonal to the front strips. This gives us a total of 256 possible hit combinations for one particle detection. We refer to combinations of front and back strips as pixels. The pixels of the DSSSD are 3 mm wide and have a 0.1 mm spacing between them. This 0.1 mm is effectively a "dead" area which is an area of the detector that does not detect any particles. The "active" area of the DSSSD is $50 \times 50$ mm. While the

design is of the "W1" type it has however been modified to be able to detect very low energy $\alpha$ particles. In table 3.1 the thickness and dead layer of the detectors is presented. A dead layer (similar to a dead area) is a layer of material on the top/bottom of the detector, that does not detect any particles. Normally this dead layer is due to Aluminium strips situated on the front of the detector. The purpose of these strips is to generate an electric potential to "disperse" electron-hole pairs for measurement, as known from a regular silicon detector. However regular W1 type design has a dead layer of $\approx 630$ nm, where the modified version has around 100 nm. This is achieved using an Al grid and contacts, instead of the regular Al strips. How can such a minimal change have a big effect? For an $\alpha$ particle with 1 MeV, the energy loss is $\approx 200$ keV for the original design, but only 31 keV for the modified design on average. This calculation for this little example was done with the SRIM package [26], with the method presented in section Energy Loss. The PAD's have the same dimensions as the DSSSD's but with no segmentation. They act as a big stopping block to measure all particles that went through the DSSSD. This is mostly $\beta$ particles.

The dead layers listed in table 3.1 can have two origins. If uncertainties are provided, then the value has been measured in the previous work [1]. If no uncertainty is noted then it is the dead layer thickness provided by the manufacturer.

| Detector name | Thickness($\mu$m) | Dead layer (nm) | Type |
|---|---|---|---|
| U1 | 42 | 115(6) | DSSSD |
| U2 | 67 | 132(13) | DSSSD |
| U3 | 1041 | 100 | DSSSD |
| U4 | 524 | 114(11) | DSSSD |
| U5 | 69 | 100 | DSSSD |
| U6 | 65 | 94(11) | DSSSD |
| P1 | 505 | 600 | PAD |
| P4 | 1473 | 600 | PAD |
| P6 | 1483 | 600 | PAD |

**Table 3.1:** *Overview of the different detectors used in the setup. Here DSSSD refers to double-sided silicon strip detector and PAD to silicon pad detector. The thickness and front dead layer of each detector are given. Note the numbers without uncertainties are factory expected thicknesses, where the numbers with uncertainties are from measurements carried out in [1].*

# 4 Data reductions and cuts

In this chapter, we will discuss how data is reduced and sorted in this experiment. From sorting the raw data to identifying the triple $\alpha$ coincidences. Throughout this chapter, we have used the software *Ausalib* [27], to automate energy loss calculations, sorting data, calibrations etc. Whenever the software has been used throughout this work, it will be explained how it performs the different tasks.

## 4.1 Calibration

The calibration used in the work presented in this masters thesis has its origin from the previous work on this experiment. Therefore to learn more about the calibration method used in this experiment, we refer to section 5 of [1]. The measurements of the calibration source with peaks described in table 5.1, have been checked to verify the quality of the calibration. An example of this, together with other information, can be seen in figure 5.1. While this figure is used in another context, the data graph is from the calibration of U1, and the vertical line indicates the tabulated peak values for the $\alpha$ source.

## 4.2 Matching

After we have calibrated our data, we need to match the hits to each other. Our DSSSD is as the name indicate double-sided. We need to match hits in the front strips, with hits in the back strips. When this is done, we will know what pixels the particles hit and can continue to calculate the energy of the particles $E = 1/2(E_f + E_b)$, as the average energy of the front and back strips. However, there are many special matching cases we need to consider.

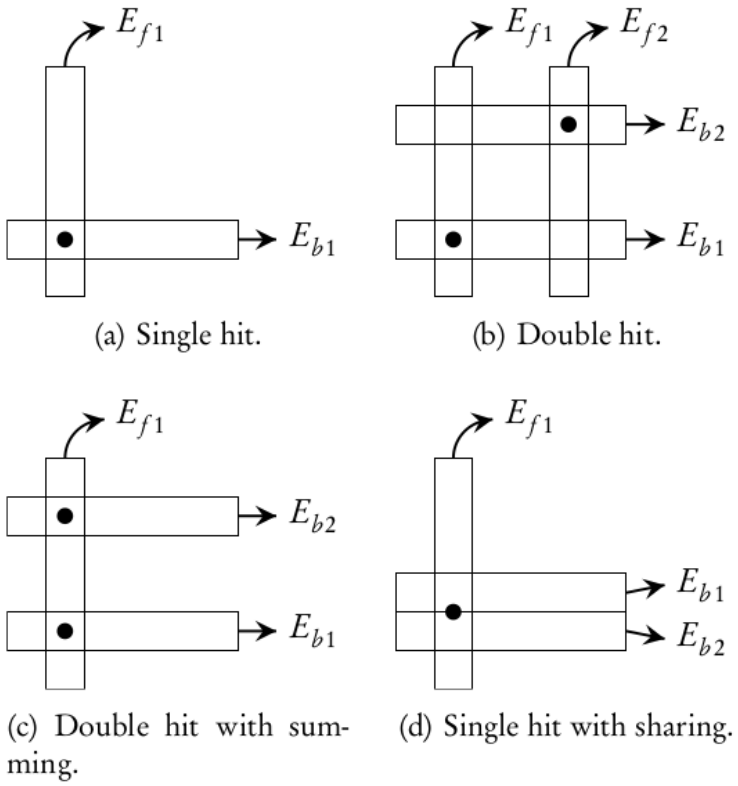


**Figure 4.1:** *Overview of different special cases that can occur when matching particle hits in the front and back strips of a DSSSD. Further description of the figure can be found in the text. The figure is taken from [1].*

These cases are presented in figure 4.1. The first case figure 4.1(a) is the simplest one. Here one particle hits the detector and we can easily identify the event and its energy. In 4.1(b) two particles hit our detector. That means that we have to possible combinations of front

and back matching. Here we choose the combinations with the lowest difference in energy between the front and back hits $E_{f,i} - E_{b,j}$, where i,j is the index of the front and back strips. Some of the rarer events are shown in 4.1(c) and 4.1(d). In 4.1(c) we have charge summation in one of the strips. That is when two particles hit the detector, and the two front(or back) strips deposits are summed into one strip. We then have one front(back) hit and two back(front) hits. Here we split the front strip energy:

$$E'_{f1} = (E_{b1}/(E_{b1} + E_{b2}))E_{f1} \text{ and } E'_{f2} = E_{f1} - E'_{f1} \tag{4.1}$$

After which we match as in case (b). The last case 4.1(d) is charge sharing. The pixels in our DSSSD has a little gap between each other. The gap size is 0.1 mm. When a particle hits this region, the neighbouring pixels can share the charge carriers. There is no way for us to identify these events, from charge summing. We, therefore, ignore every event combinations where neighbouring strips have detected a hit. The amount of data where charge sharing occur is similar to the relative area of the pixels and gaps. With a gap size of 0.1mm with pixels of 3 mm width, we expect charge sharing to account for 3 % of our data.

## 4.3 Energy Loss

When analysing the data from the $^{12}$N decay (2.1), it is important to remember that the measured energies in our detectors are always too

small. This is because the particles lose some of their energy when travelling out of the target foil, and through the "dead layer" on the front of our detectors. To correct for this energy loss we use the Ausalib software [27]. Ausalib makes use of the SRIM package [26], which includes a tabulation of the depth different ions travel in a chosen material for a given energy. We can e.g. find how deep a 5 MeV $\alpha$ particle will penetrate silicon material that is 500 nm thick. By using cubic spline interpolation we can create a continuous energy range function $R(E)$. Here the cubic spline interpolation basically creates a polynomial that interpolates ranges for energies not tabulated. We can write:

$$R(E_i) = R(E_f) + \Delta x_d \tag{4.2}$$

Where $E_i$ is the initial energy of the $\alpha$ particle, $E_f$ is the final energy and $\Delta x_d$ is the thickness of the material. We can then find the inverted function $R^{-1}(E_i)$, since $R(E_i)$ is monotonic, so we obtain the initial energy of the particle.

$$E_i = R^{-1}(R(E_f) + \Delta x_d) \tag{4.3}$$

We know from the previous work [1], that the $^{12}$N will have a close to Gaussian distribution throughout the target foil. It was estimated(in figure 4.3 in [1]) that the peak position of this distribution was at 64 nm implementation depth in the target foil. That is to say, that we assume in the analysis that every decay took place at 64 nm implementation depth. This assumption will also be tested in the simulation section, where we simulate decays with varying implementation depth to compare with data.

## 4.4 Identify triple-$\alpha$ and double-$\alpha$ events

### Triple-$\alpha$

Now that we have finished the matching of our events and identified how to calculate the energy loss in our setup from various sources, we must now address how to find the triple-$\alpha$ coincidences (and double $\alpha$ later). We start by only looking at events with 3 hits or more. We then calculate the total momentum for all possible configurations of three hits. The configuration of hits with the lowest total momentum is assumed to be triple-$\alpha$ particles. If any hits were detected that had an energy deposit in both a DSSSD and a PAD, they are marked as possible $\beta$ particles. From this selection, we can draw a total momentum vs total energy scatter plot, as shown in figure 4.2.

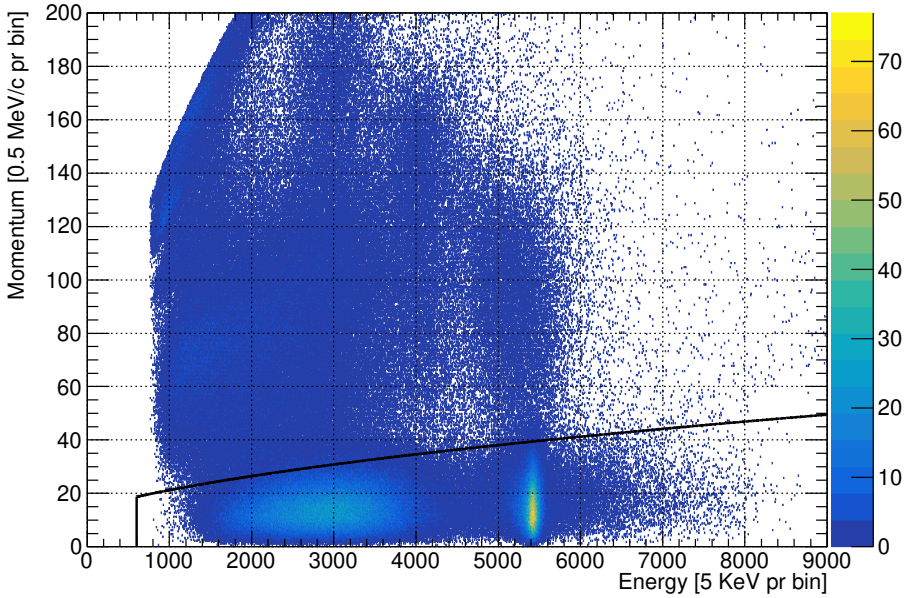


**Figure 4.2:** *Total momentum vs total energy of a triple-$\alpha$ coincidence event. The black line represents a momentum energy cut in which the real triple-$\alpha$ events should be under the line. The cut is described in equation* (4.4)

In figure 4.2, we expect the true triple-$\alpha$ decays to have the lowest momentum. Theoretically, it should be 0 if we assume that $^{12}$N lies perfectly still inside our foil. However in reality we have uncertainty from imperfect energy loss corrections from the foil and dead layer of our detectors. Also, the pixel width of our DSSSD is 3 mm which gives rise to an angle uncertainty as well. It is therefore of no surprise that our triple-$\alpha$ events have total momentum different from 0. The

higher momentum events in figure 4.2, mainly arise from events where we accidentally find two $\alpha$'s and one $\beta$. We can make an energy-momentum cut in figure 4.2 to discard these events. In previous work on this experiment [1] the momentum energy cut of equations 4.4 have been used.

$$|\sum_{i=1}^{3} \mathbf{p}_i| < \frac{1}{2}\sqrt{\sum_{i=1}^{3} E_i + 800\,\text{keV}} \text{ and } \sum_{i=1}^{3} E_i > 600\,\text{keV} \tag{4.4}$$

Equation (4.4) is not derived from any theoretical work, but is found from experience to work very well. The cut has been drawn as a black line in figure 4.2. The structure we see in figure 4.2 below the cut resembles that indicated from the level scheme in figure 2.1. The narrow hot spot around 5425 keV, corresponds to decays through the $1^+$ excitation state in $^{12}$C:

$$^{12}\text{N} \rightarrow^{12} \text{C}^*(1^+) + \beta + \nu_e \rightarrow^{8} \text{Be}^*(2^+) + \alpha \rightarrow \alpha + \alpha + \alpha \tag{4.5}$$

The broader hotspot between 1500-4500 keV arises from decays to the ground state $0^+$ of $^8$Be. Generally, all the decays to the $^8$Be ground state, that can arise from $^{12}$C excitation energies between the triple $\alpha$ threshold (7274 keV) and the $\beta$ window (16315 keV), can be seen in this broad signal. Many of these structures have been covered and discussed in previous work [1]. The same resonances can be seen in the total energy plot in figure 4.3. The $1^+$ $^{12}$C peak is located at 5425.6(4) keV with a FWHM of 122 keV.

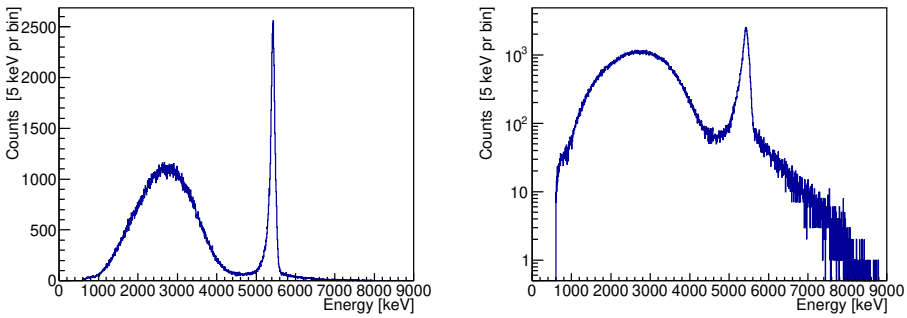


**Figure 4.3:** *The total energy of three $\alpha$ particles from the reaction in equation (2.1). In linear and logarithmic scales respectively.*

In table 4.1 we give an overview of how the different cuts have decreased the amount of data. From this table it is clear that the biggest impact on the data is the momentum-energy cut from equation (4.4). This motivates the analysis of double-$\alpha$ coincidence analysis. If we can reconstruct the lost information when we only detect two $\alpha$'s there is a large potential of additional data to gain. If we can understand the error we induce in reconstructing $\alpha$ particle data there may be a big net gain in statistical precision. The decay channels through the $^8$Be ground state and excited state is separated with an energy cut in relative energy of the two lowest energy alphas $E_{23}$. This can be calculated since we already have the momentum vectors of $\alpha_2$ and $\alpha_3$. We can find the energy in their common centre of mass system with:

$$E_{23} = 2\frac{\vec{p}_{23}^{\,2}}{2m_\alpha} \text{ and } \vec{p}_{23} = \frac{1}{2}(\vec{p_2} - \vec{p_3}) \tag{4.6}$$

A plot of $E_{23}$ can be found in figure 4.4. The sharp peak at 92.34(3) with a FWHM at 39 keV is the $^{8}$Be ground state peak. At larger $E_{23}$ the spectrum rises again, representing all the decays through the $^{8}$Be excitation state. The cut off as indicated in figure 4.4 is chosen at 250 keV.

| Cuts | No. of events |
|---|---|
| Event multiplicity >2 | 21563015 |
| momentum and energy cut | 522823 |
| Be-groundstate | 393506 |
| Be-excitation | 123745 |

**Table 4.1:** *Overview of how different data cuts affect the total amount of events available for triple-$\alpha$ coincidences.*

## Double-$\alpha$

As mentioned in the previous section the motivation for analysing two-$\alpha$'s coincidence is to gain a larger uncorrelated data set. Let us first look at events with two detector hits to see what we can gain from this (in contrast to finding two $\alpha$ candidates from 3 hits). So we only take events with 2 hits detected and assume those are $\alpha$'s. From the conservation of momentum, we calculate what direction and energy the missing alpha should have to give total momentum 0. We then plot the total energy of the three $\alpha$'s, as shown in figure 4.5. We see in figure 4.5 the $1^{+}$ excitation peak(at $5-6$ MeV) as we have seen earlier from the triple $\alpha$ coincidence plot of figure 4.3. Besides that, we see a

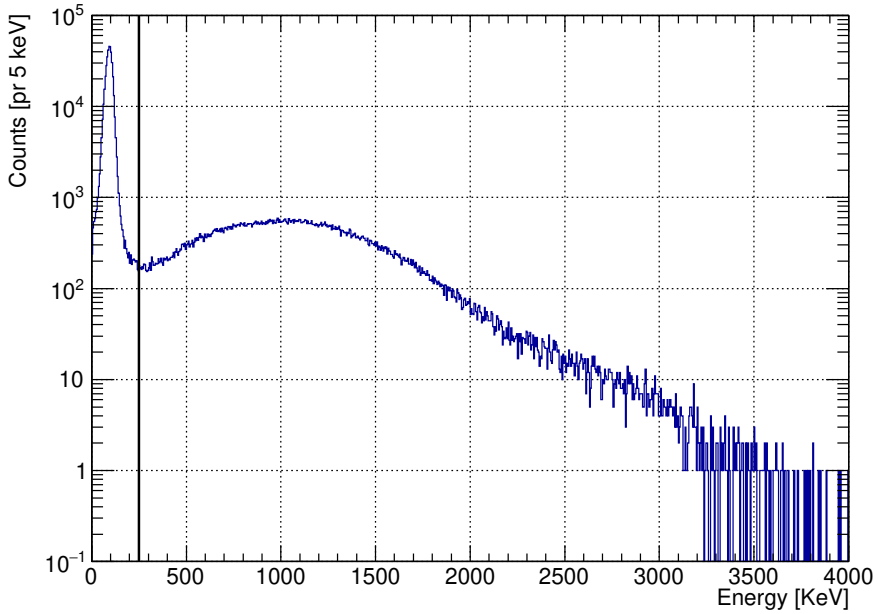


**Figure 4.4:** *The relative energy of the two lowest energy $\alpha$ particles $a_2$ and $a_3$. The black line at 250* keV *indicates the border between* $^8$Be *ground state decays ($E_{23} < 250$keV) and decays through the* $^8$Be *excitation state($E_{23} >$* 250keV*).*

major peak in the 1-4 MeV interval. However, the intensities between the broader peak at 1-4 MeV and the $1^+$ peak are very different. Also, a new peak around 1 MeV is visible. This is somewhat expected since the biggest issue in reducing the data is to avoid the case where we find one $\alpha$ and one $\beta$. These cases have the largest contribution at lower total energy since the $\beta$ particles have lower energy compared to

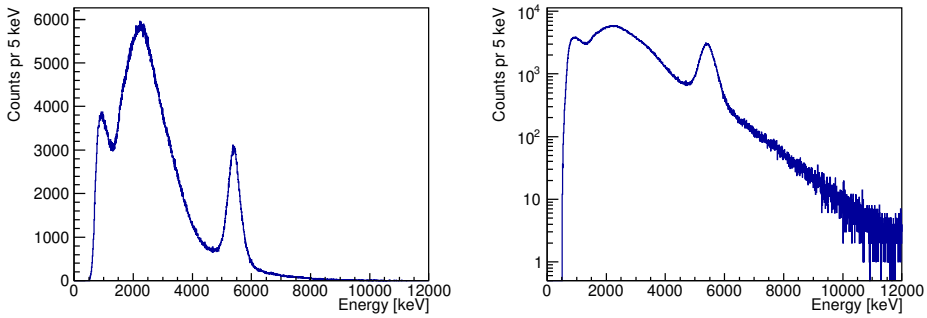


**Figure 4.5:** *The total energy of double $\alpha$ coincidence events. Here the third alpha is reconstructed based on conservation of momentum. The data has been plotted in linear and logarithmic scales respectively.*

the $\alpha$ particles in these decays. To clean up this data set, we have to make two data cuts. The first is to discard all the data where a hit is detected in both a DSSSD and the PAD behind it. Since our thinnest DSSSD U1, with a thickness of 42 $\mu$m, should stop all $\alpha$'s under 7 MeV, we assume any hit in both DSSSD and the PAD is a $\beta$. The second cut relates to the direction of our reconstructed $\alpha$ particle. We assume that if the reconstructed $\alpha$ has a direction which is into a detector, we would have detected it already. To evaluate this cut, we can plot the polar angle $\theta$ and the azimuthal angle $\phi$ of the reconstructed $\alpha$. Such a plot is shown in figure 4.6. Here we see three heat spots, however, spots at $\theta \approx 90$, $\phi \approx 180, -180$ are linked together and are in the beam direction (z-direction). The spot at $\theta \approx 90$, $\phi \approx 0$ is in the -z-direction. We find that most of the lost $\alpha$ particles go in the beam direction or the opposite to that. The shapes drawn onto figure 4.6

indicates where detectors are located. So hits inside these areas are discarded. There are also some bright spots around $\theta \approx 90 - 120$, $\phi \approx 50, 150$. This is expected since decays through the $^{8}$Be ground state often produce a high energy $\alpha$ and two low energy $\alpha$'s from the $^{8}$Be break up, that is they go in opposite directions. This indicates the cases where we detect two low energy alphas in the U5 DSSSD and detect no high energy alpha in $\theta \approx 90 - 120$, $\phi \approx 50, 150$ since no detector is placed here.

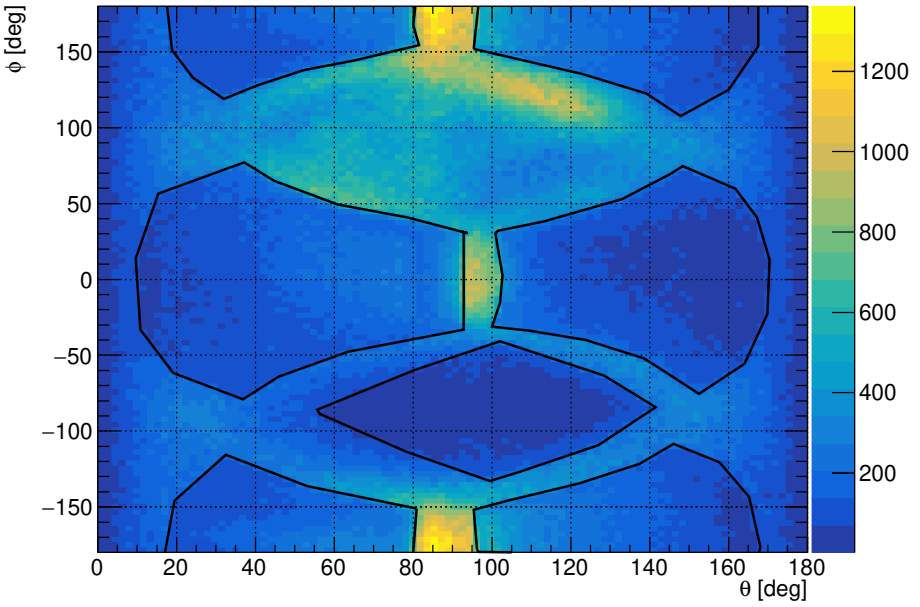


**Figure 4.6:** *The azimuthal angle $\phi$ and polar angle $\theta$ of the reconstructed $\alpha$ particle from the double-$\alpha$ coincidence analysis. The shapes drawn with a black line indicates where a detector is located.*

After making both of these cuts we can plot the total energy once again. Such a plot is shown in figure 4.7. This compares much better to the triple $\alpha$ total energy plot from figure 4.3. The $^{8}$Be ground state peak between 1-4 MeV is still a little skewed to the left, which indicates that we did not discard all the fake alpha events, but the overall result is a lot better. A discussion of the peak broadening and general smearing of the double-$\alpha$ coincidence data follows in section 4.7 (and in the simulation section 5.2) where we make the double-$\alpha$ analysis on the triple-$\alpha$ analysed data. In table 4.2, we present the remaining events after each cut. The cuts accumulate so that row two have the cuts of both row 1 and 2 and so forth. Here two things are important to notice. Firstly, after performing the two cuts presented above, we still have 859036 events left. If we compare that to table 4.1(Same table but for triple $\alpha$ coincidences), that is an $\approx 66\%$ increase of data available. Secondly, we have more data of the $^{8}$Be excitation decay channels than in the $^{8}$Be ground state decay channels, wherein the triple analysis it is opposite. As previously mentioned, this is expected since in the decays through the $^{8}$Be ground state the high energy $\alpha$, and the two low energy $\alpha$'s should be moving in opposite directions. Since the detectors are placed in opposition (except U5) we expect that if one is detected the other should be as well. However, for decays through the $^{8}$Be-excitation state, the angles between the three $\alpha$'s are more "arbitrary", so the double-$\alpha$ is more useful here. This is further studied in the simulation section 5.4, where we calculate the acceptance of the triple and double $\alpha$ analyses for different decay types.

In figure 4.7 we see the same overall structures as in the corresponding energy plot for the triple coincidence analysis in figure 4.3. The $1^+$ peak is located at 5419.3(7) keV with a FWHM of 522 keV. This is $\approx 4$ times bigger than the FWHM measured from the triple coincidence analysis. Also, the peak position has been shifted down 5 keV, which is not a lot compared to the quality of calibration (which is also around a 5 keV resolution) but still noticeable.

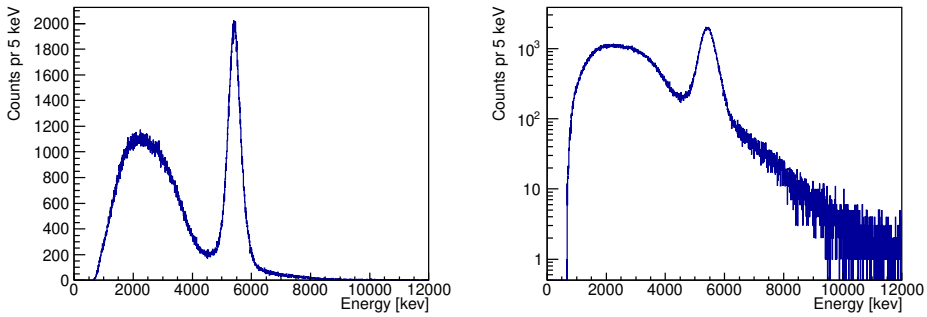


**Figure 4.7:** *The total energy of double $\alpha$ coincidence events. Here the third alpha is reconstructed based on conservation of momentum. We plot the data with a linear y-axis(left) and log(y) axis(right).*

## 4.5 Determination of the foil thickness

In the original work of Jonas Refsgaard [1] the foil thickness was measured. This was done before the experiment started and after it was finished. The method to determine the foil thickness was to measure the energy of a known calibration source first with the foil in front of

| Cuts | No. of events |
|---|---|
| Event multiplicity = 2 | $23.13523 \cdot 10^6$ |
| No beta allowed | $1.64768 \cdot 10^6$ |
| Direction | 859036 |
| Be-groundstate | 386386 |
| Be-excitation | 472650 |

**Table 4.2:** *The number of events remaining after each data cut. The cuts accumulate, where the first row includes cut one and the second row includes cuts one and two etc.*

the source and then without the foil. From the shift of position of the peaks in the two measurements, you can infer a foil thickness. The results of these measurements are in table 4.3. From table 4.3 it ap-

| Runs | $\Delta x_f$ (nm) |
|---|---|
| 66 and 68 | 96(4) |
| 294 and 314 | 123(3) |

**Table 4.3:** *Measurement of the foil thickness from before and after the experiment. The data is divided into runs where the experiment goes from run 70 to run 290. $\Delta x_f$ is the foil thickness. Data is taken from [1].*

pears that the foil thickness is increasing throughout the experiment. So a linear interpolation of the foil thickness was originally made in relation to the run time. We will now test if we can find evidence of such an effect. Since the data is split up in many consecutive "runs" we can look for any accumulating effects. If we locate the position of the well determined $1^+$ peak of $^{12}$C for each run, we can see if the

position changes accordingly for increasing runs. We analyse the data first with a fixed value of the foil thickness and then with a thickness that increases linearly with the run number. For each run, we find the bin $x_0$ with the highest count value between 5000-5800 keV and fit a Gaussian function in the range [$x_0$-120keV, $x_0$+120keV]. An example of such a fit is given in the appendix, figure 6.9. The results of these fits are shown in figure 4.8 and figure 4.9.

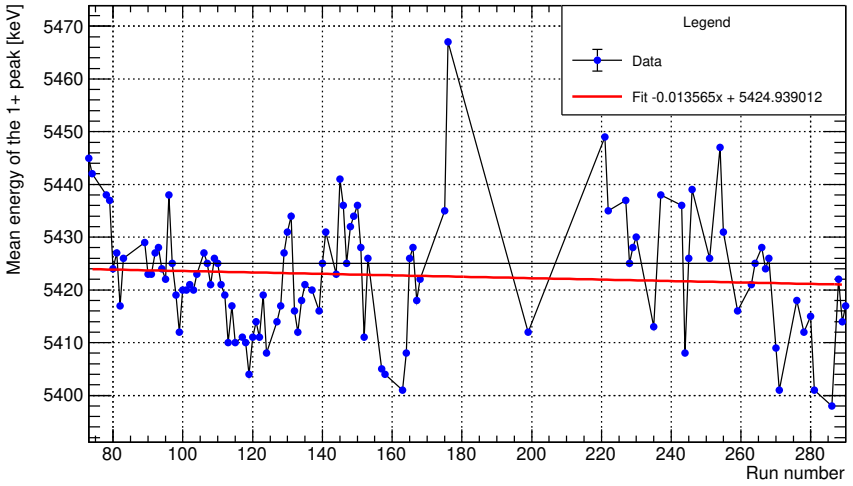


**Figure 4.8:** *Positional changes of the* $1^+$ *peak in* $^{12}C$ *vs the run number (described in the text). Data is analysed with a fixed foil thickness of 96 nm. The black line at* 5425 keV *is graphed to show the measured value of the peak position for the whole data set with 96 nm foil thickness. The red line is a linear fit to the data.*

In figure 4.8 we see the fits for a fixed foil thickness of 96 nm. The

error bars are not shown here since they are rather large, $\sigma \approx 70$ keV, and would disturb the clarity of the graph. Furthermore only runs with more than 1500 events in the energy range of 5000-5800 keV have been included to ensure the fits are of a good enough quality. A linear function has been fitted to evaluate any increasing/decreasing tendencies. From this fit, we can see that there is a slight downward drift for increasing runs. This implies that the energy loss correction of the foil is too small for increasing run numbers. That is to say that the foil thickness is growing and the energy loss correction is staying the same. Since the errors of the points are around the $\sigma \approx 70$ keV, it is difficult to say for sure that such a small drift is a significant increase of the foil thickness. If we try to let the foil thickness increase from 96 nm to 123 nm linearly with the run number, we can see in figure 4.9 that we heavily induce a systematic drift in the $1^+$ peak position. More investigation is needed here to check for non-linear drift effects and possible correction methods. You could e.g. increase the foil thickness with run time and not run number since some runs are longer than others. In this work, it is assumed that the foil thickness is fixed at 96 nm in the analysis since the drift found in figure 4.8 is rather small and correcting it would have an equally small effect.

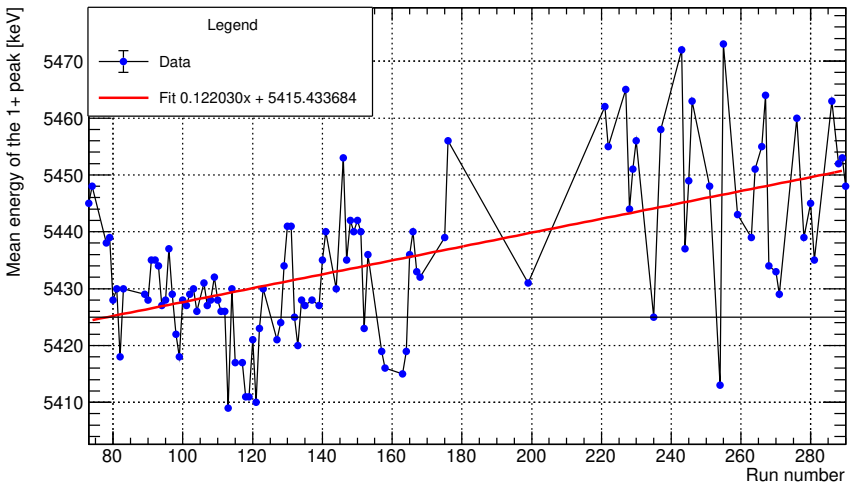


**Figure 4.9:** *Positional changes of the* $1^+$ *peak in* $^{12}C$ *vs the run number (described in the text). Data is analysed with a linearly increasing foil thickness, from 96-123 nm in contrary to figure 4.8. The black line at* 5425 keV *is graphed to show the measured value of the peak position for the whole data set with 96 nm foil thickness. The red line is a linear fit to the data.*

## 4.6 Spectra

### Fynbo plots

In the last section, we were able to produce the total energy spectrum of the triple $\alpha$ decay. We did this for the triple and double $\alpha$ coincidence analysis in figure 4.3 and 4.7 respectively. Another way to present this data is with a so-called "Fynbo" plot (named after Hans Fynbo). This is a scatter plot in which you plot the total energy on

the x-axis and the energy of the individual $\alpha$ particles on the y-axis. Such a plot is presented in figure 4.10. It should be noted, that one decay event produces three data points on this type of plot, since for each event we have one total energy and three separate $\alpha_{1,2,3}$ energies.

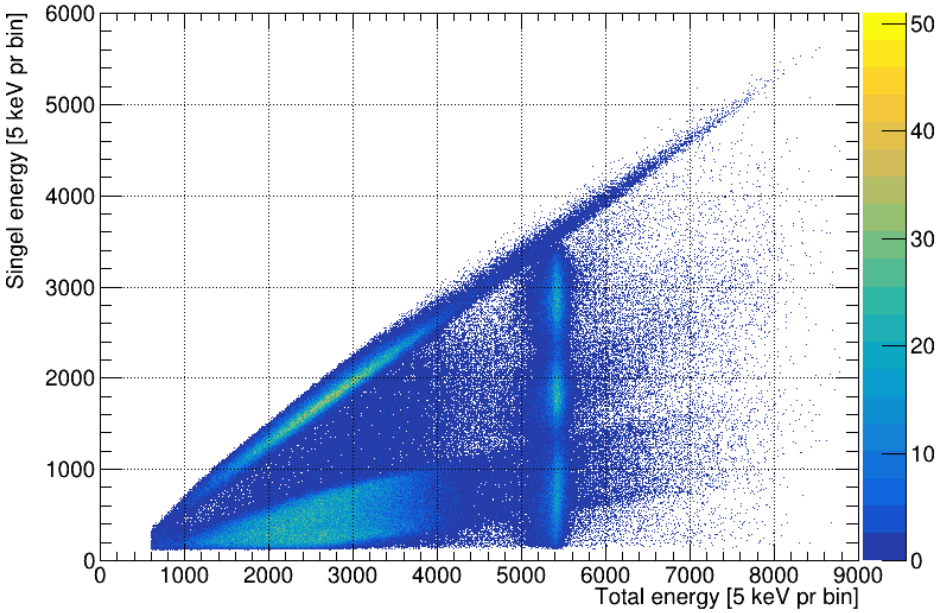


**Figure 4.10:** *The energy of the individual $\alpha$ particles on the y-axis and the total energy of the three $\alpha$ particles on the y-axis. Note that one decay event produces three points on this plot. The data is extracted with the triple $\alpha$ coincidence analysis.*

Figure 4.10 is for the triple $\alpha$ coincidence analysis. Here we see three distinctive clusters at $E_{tot} \approx 5400$. These are the decays through

the $1^+$ excited state in $^{12}$C. The two other clusters of data, that stretches over the whole spectrum of total energy, are decays through the ground state in $^8$Be. These can be isolated with the same energy cut as described in section 4.4. Namely $E_{23} < 250$ keV, where $E_{23}$ is defined in equation (4.6). The same scatter plot with this energy cut is shown in figure 4.11.

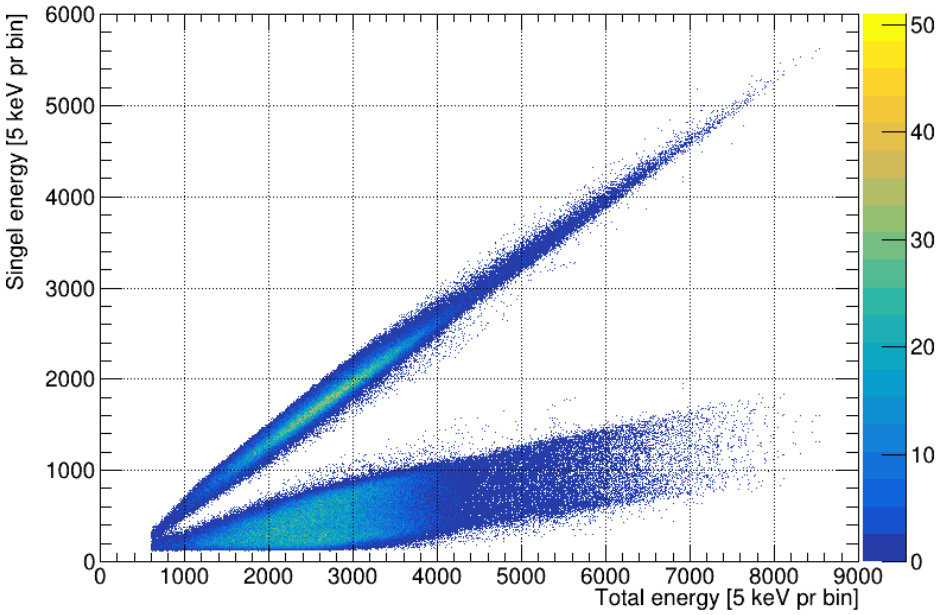


**Figure 4.11:** *The energy of the individual $\alpha$ particles on the y-axis and the total energy of the three $\alpha$ particles on the y-axis. Here an energy cut of $E_{23} < 250$ keV is used to isolate the decays through the $^8$Be ground state. Note that one decay event produces three points on this plot. The data is extracted with the triple $\alpha$ coincidence analysis.*

Here we see two energy bands. However, we do actually have a band for each $\alpha$ particle but the two bands of the lower energy $\alpha$ particles overlap and create one very broad energy band. Remember that the way we read these plots is as follows: For a given total energy e.g 3 MeV, we find the most energetic $\alpha$ particle in the upper energy band at $\approx 2$ MeV. This means that the two lower energy $\alpha$ particles are in the lower band, with an energy between 200-900 keV. You could of course also make a plot with the opposite energy cut, $E_{23} > 250$ keV, to isolate the data of decays through the $2^+$ state in $^8$Be. This is shown in the appendix figure 6.10. These Fynbo plots, have also been made for the double coincidence $\alpha$ particle analysis, and are shown in figure 4.12, 4.14 and 4.13. Figure 4.12 has the same structure as seen in figure 4.10. For the $1^+$ peak we see three clusters as expected, but with more broadening in $E_{tot}$. It is important to note that this broadening does not have horizontal symmetry. There looks to be some energy-dependent systematic effect that shifts some of the data from the $1^+$ peak to higher total energy. This effect will be investigated further in the simulation section 5.2 and section 4.7. If we take a look at figure 4.13 we also see a lot of data under the $1^+$ peak. This is mostly data from the $^8$Be ground state that does not get excluded with $E_{23} > 250$ keV energy cut. If we look at the plot for the $E_{23}$ in figure 4.4, we note that the $^8$Be ground state peak does not stop at 250 keV, but rather the $^8$Be excitation peak dominates for larger energies. You can imagine that the ground state peak continues under the $^8$Be excitation peak and diminish for higher energies. This effect is stronger for the

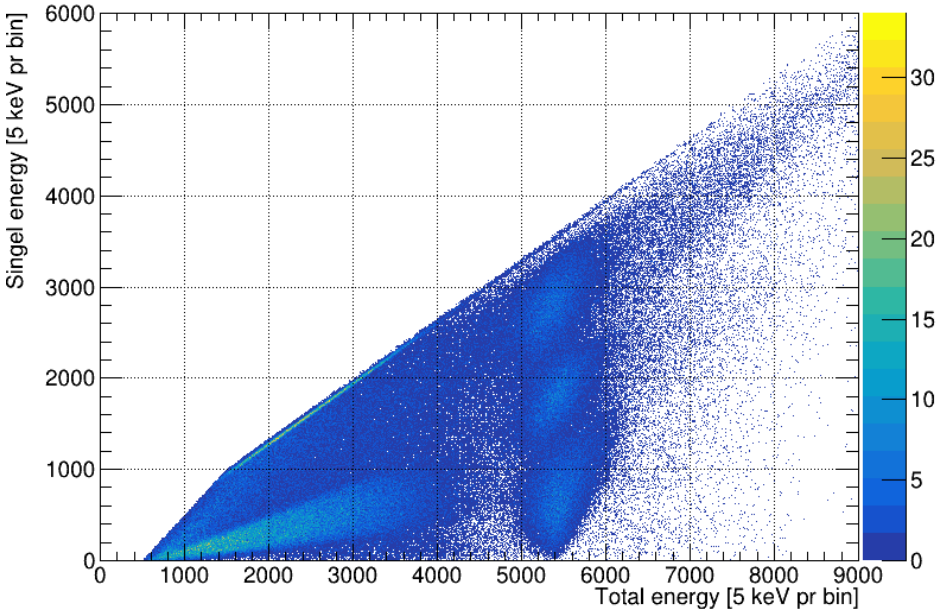


**Figure 4.12:** *Fynbo plot (see description in figure 4.10) of data extracted with the double $\alpha$ coincidence analysis.*

double coincidence $\alpha$ analysis since our energy measurement has a generally higher uncertainty (As seen in the peak broadening in e.g. figure 4.7).

The decay through the $^{8}$Be ground state is seen in figure 4.14. Here the most striking feature is the very sharp energy band for the most energetic $\alpha$ particle. Also the energy bands for the two lower energy $\alpha$'s has been narrowed. Of course, the narrowing of these bands should not be interpreted as an increased precision, but rather a loss in precision

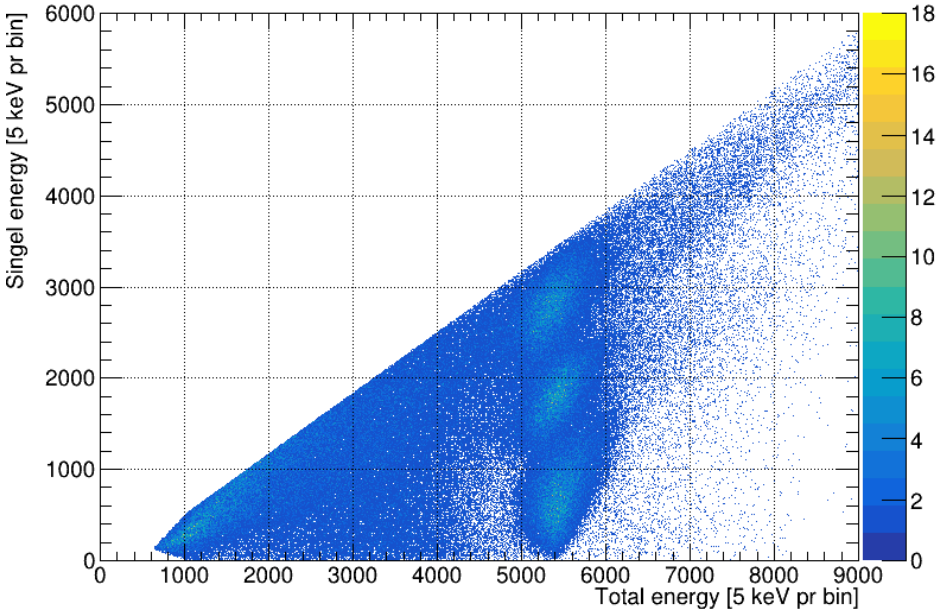


**Figure 4.13:** *Fynbo plot (see description in figure 4.10) of data extracted with the double $\alpha$ coincidence analysis. Here the decays through the* $^{8}$Be $2^{+}$ *state is isolated with the energy cut* $E_{23} > 250$ keV

due to forcing the total momentum to be 0.

## Dalitz plots

In section 2.2, we discussed Dalitz plots and why they were useful to present data of decays with three fragments in the final state. With coordinates as defined in equation (2.5), we present the Dalitz plots from the triple $\alpha$ coincidence analysis in figure 4.15 and the double $\alpha$

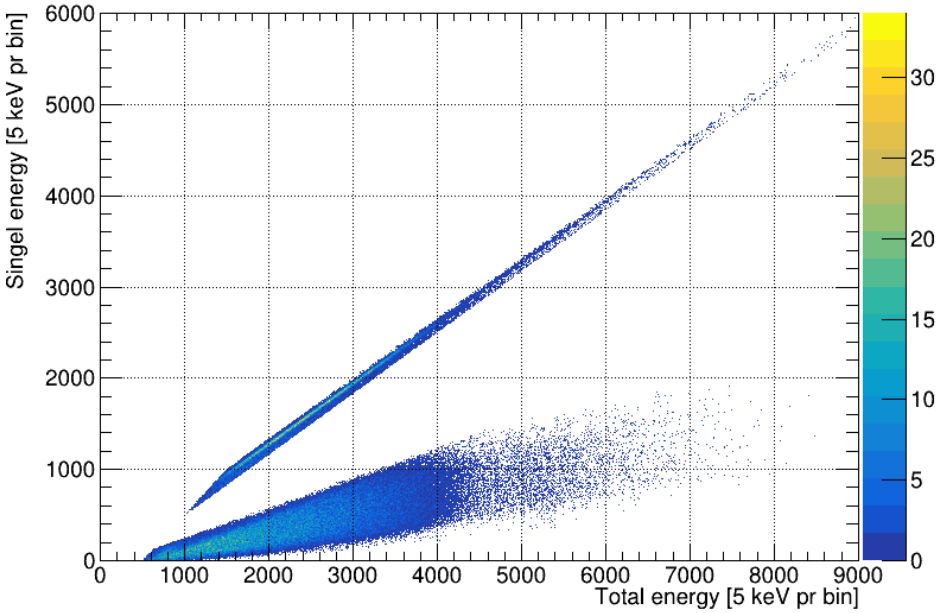


**Figure 4.14:** *Fynbo plot (see description in figure 4.10) of data extracted with the double $\alpha$ coincidence analysis. Here the decays through the* $^{8}$Be *ground state is isolated with the energy cut* $E_{23} < 250$ keV

coincidence analysis in figure 4.16. It is tempting to interpret these plots based on the theoretical expectations of different decay modes from figure 2.3 and 2.4. However, without acceptance corrections, it is not possible to interpret any signal as evidence of a given decay mode. By acceptance, we mean our detector and geometrical acceptance. Based on our detector and how they are placed, different alpha decays might be more or less probable to detect. This could e.g. be seen

as bright and dim spots from uniform phase space distributed events in our Dalitz plots. A strong signal would then be overestimated and vice versa. In section 6.5 we calculate this acceptance from simulations and apply the correction to our Dalitz plots. What we can do now, is compare figure 4.15 to the earlier work in figure 6.8 in [1]. What we see there is a definite agreement with the earlier work. All the Dalitz plots in figure 4.15 resemble their corresponding plot in figure 6.8 in [1]. That we can reproduce earlier work, indicates that our method is correct, in the sense that two independent analyses give the same result. Or that we made the exact same mistakes (hopefully not).

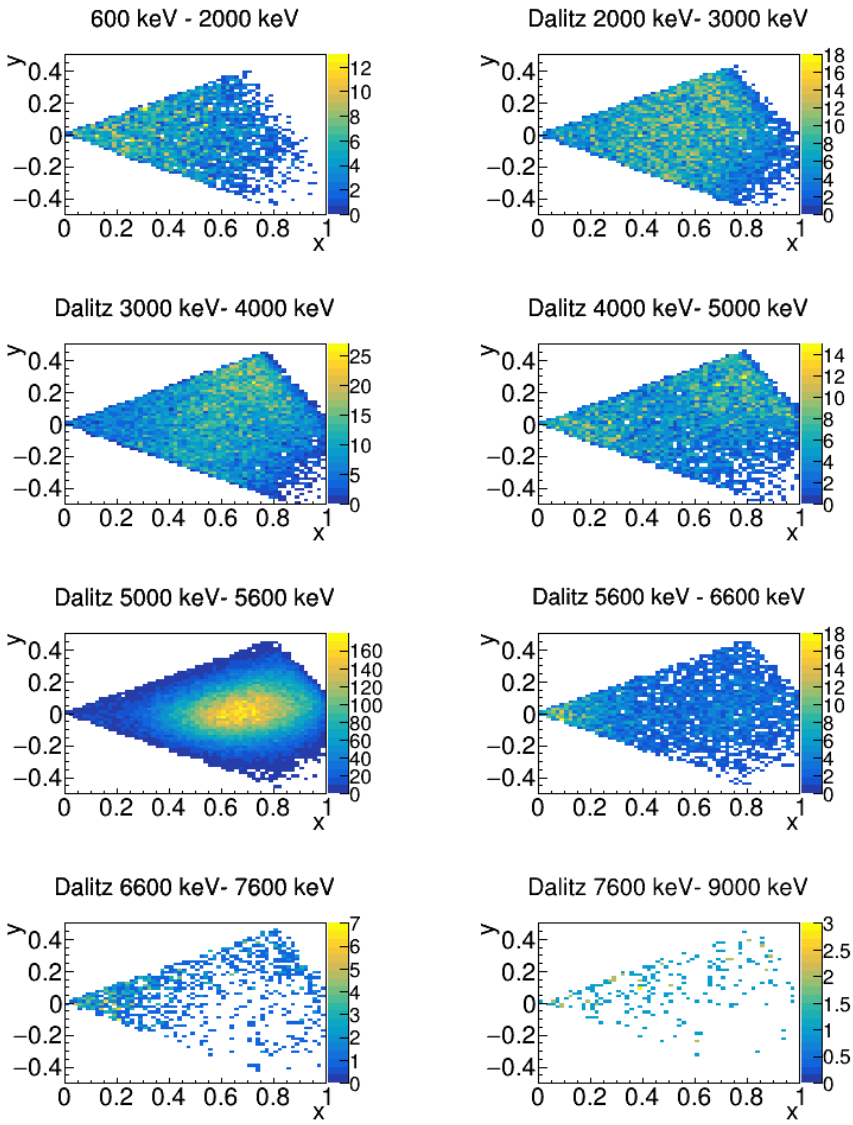


**Figure 4.15:** *Dalitz plots of the triple $\alpha$ coincidence analysis with $E_{23} >$ 250 keV. The binning is $60 \times 60$ and the total energy range is written above each of the plot. x- and y-coordinates are defined as in (2.5).*

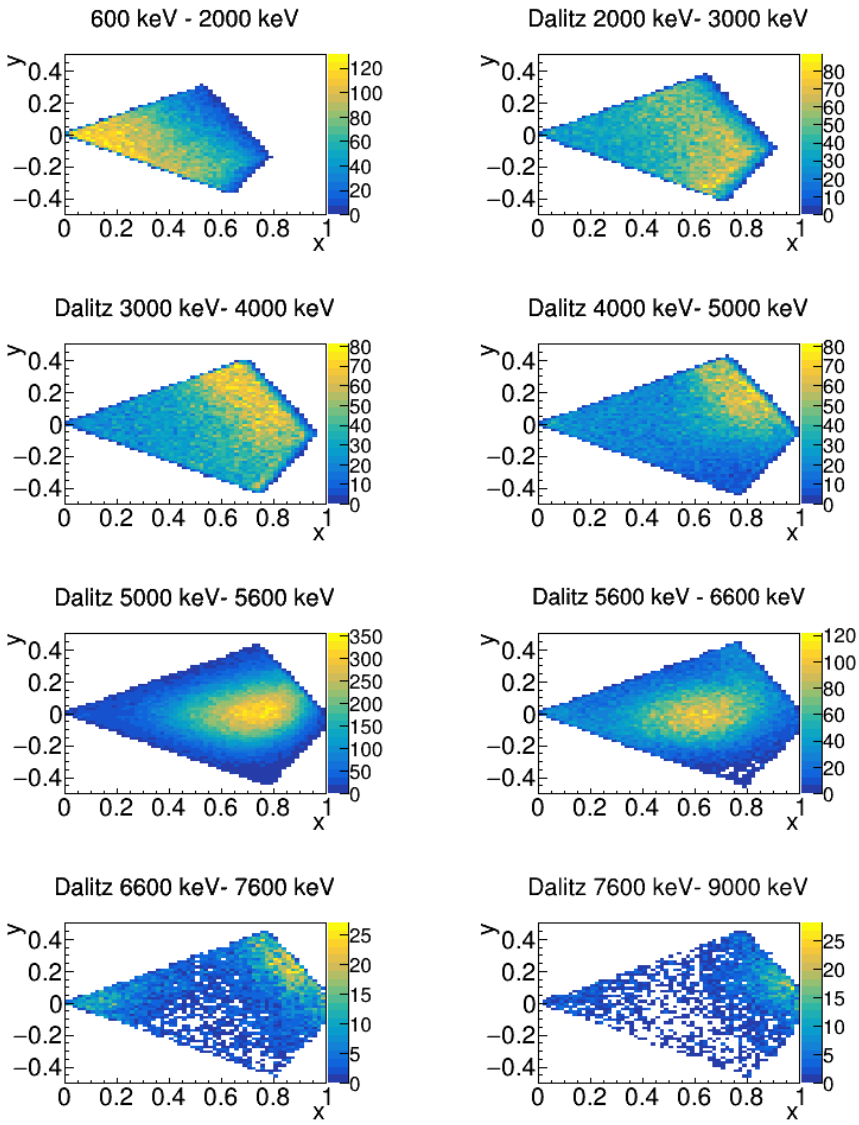


**Figure 4.16:** *Dalitz plots of the double $\alpha$ coincidence analysis with $E_{23} >$ 250 keV. The binning is $60 \times 60$ and the total energy range is written over each plot. x- and y- coordinates are defined as in (2.5).*

## 4.7 Reconstruction of triple $\alpha$ coincidence data.

To investigate how the reconstruction of $\alpha$ particles affects our data, we try to reconstruct a known $\alpha$ particle and observe the changes it induces. That is to say, for each event where we find three $\alpha$ particles, we "remove" a random $\alpha$ and then reconstruct its information. We can then see how that affects our angle, energy and hence momentum resolution. A *Fynbo* scatter plot, similar to figure 4.10, has been made from this reconstruction method. It is plotted in figure 4.17. From figure 4.17 we see the same energy broadening as first observed in figure 4.12. However the asymmetric broadening around the $1^+$ peak (which decays through $1^+$ state in $^{12}$C) does not seem to be reproduced. We will discuss this later in the section 5.2. The FWHM of the $1^+$ peak is 207(1) keV and the peak position is 5411.2(8) keV. The effect of reconstructing a random $\alpha$ particle is therefore a shift in the peak position ($\approx$ 14 keV) and a broadening of 70 % (FWHM was originally 122 keV). The additional FWHM up to 522 keV that is observed can therefore not be explained on reconstruction alone. Furthermore there seems to be an effect that shifts the peak position to a higher energy, which mitigates the original down shift from the reconstruction. The angular resolution is tested by calculating the angle between the momentum vector of the measured $\alpha$ and reconstructed $\alpha$. A plot of this can be seen in figure 4.18. If we fit a landau function to this histogram we find a mean peak value of 6.53(2)° with $\sigma = 3°$. An

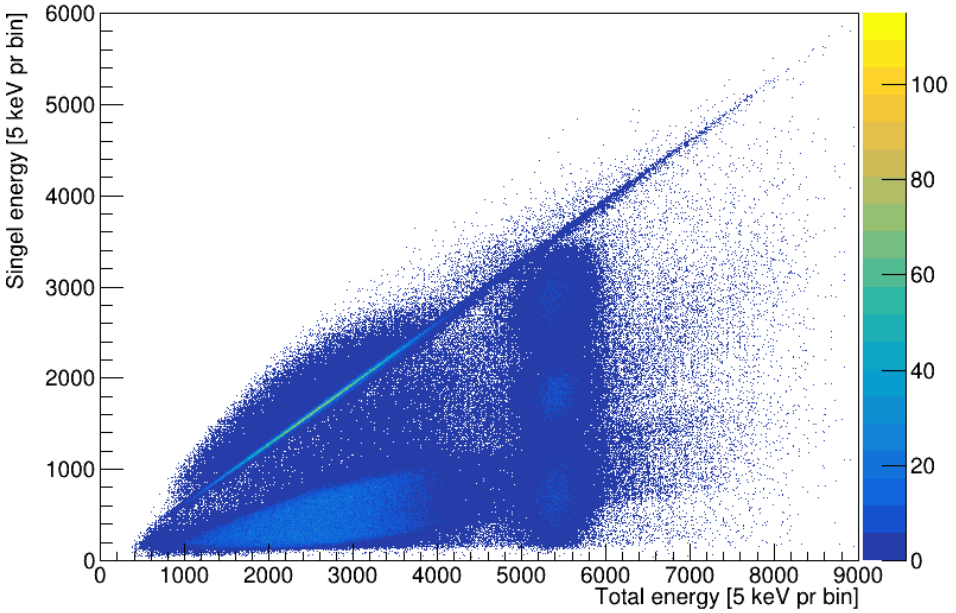


**Figure 4.17:** *Same plot as figure 4.10 where one of the $\alpha$ particles has been "removed" and reconstructed based on conservation of momentum.*

angular uncertainty of 6.5° is still small enough to be useful for $\beta$-$\alpha$ angular correlation studies, since the non-isotropic behavior studied in [14] is observed on a resolution of 3.5°. Here I refer to the binning of figure 5.20 in [14].

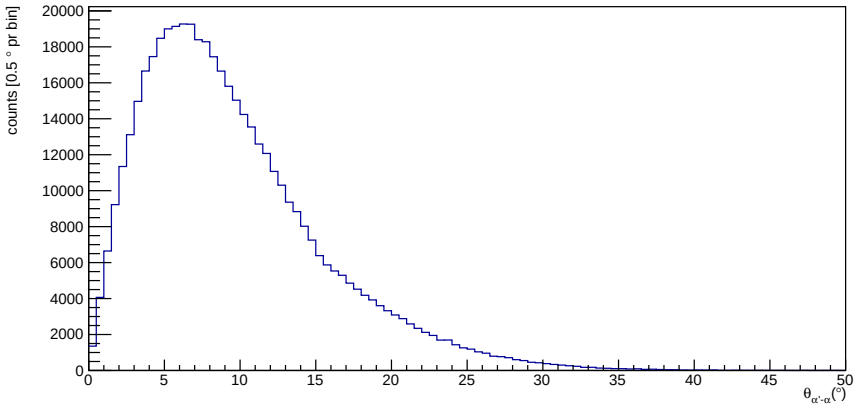


**Figure 4.18:** *Angle between a measured $\alpha$ particle and a reconstructed $\alpha$. Here the reconstructed one is based on conservation of momentum*

# 5 Simulation

*So we beat on, boats against the current, borne back ceaselessly into the past.*

The Great Gatsby - F Scott Fitzgerald

While the spectra presented in the previous section includes a lot of information about our experiment, it is with simulations that we can truly test our understanding of the physics in said experiment. In this chapter, we will perform several simulations of different decay channels from figure 2.1 and compare them with the data. With the *GEANT4*

[28] framework, we are able to perform Monte-Carlo simulations of $\alpha$ and $\beta$ particles from calculations of equation (2.6). Furthermore, the detector geometry and the frames our PADs are situated in can be simulated as well. That means we can include $\beta$ back-scattering effects. With *GEANT4* we can simulate how different foil implantation depths and beam sizes affect our data. We will analyse the acceptance of both the double and triple $\alpha$ coincidence analysis for different decay channels.

## 5.1 Software

As mentioned earlier the simulations are carried out with the *GEANT4* software made at CERN [28]. While we use version 1.0, the software has been modified by the Aarhus subatomic group under the name *G4SIM*[1]. The calculations of the decay weights are done with equation (2.6) to predict the behaviour of the $\alpha$ and $\beta$ particles. This calculation was not done in G4SIM, but rather in the software *SIM3a*[2] which was developed for the work done in [1]. This software was used to generate particle events, that could then be simulated in G4SIM. The reason for this was simply to reduce human error. SIM3a was already well tested and capable of outputting raw event files based on equation (2.6) but also including $\beta$-$\nu$ recoil effects (described in section 7.1 in [1]). In recent work [29] the frames surrounding the PAD and the Al contacts

[1] https://gitlab.au.dk/au479664/G4Sim
[2] https://gitlab.au.dk/ausa/sim3a

on top of the DSSSD have been added to G4SIM. From the inclusion of the frames we expect to be able to simulate $\beta$ back scattering effects. The Al contacts cover 3 % of the active area on the front of our DSSSD's. That means 3 % of our data experience a higher energy loss than expected. This will result in physical satellite peaks in our energy spectrum (here physical implies that the satellite peak is a consequence of a physical disturbance), with a lower energy than our main peaks. We use the *Low Energy Electromagnetic Physics - Livermore* [3] physics package from Geant4 since it gives good results for low energy particle decays. Compared to the *SIMX* used in previous work [1], *Geant4* has the possibility to simulate $\beta$ particles as well. Where earlier real-world $\beta$ noise was mixed into the simulation. Furthermore, the *GNU-PARALLEL* software [30] was used to run the simulations in parallel to speed up the process.

## Electronic noise simulation

When doing our simulations we of course would like it to replicate reality as well as possible. One of the things to consider in this regard is the electronic noise in our experiment. Our electronic equipment and cables induce noise in our experimental measurements. This noise signal can be included in *G4Sim*. To estimate our electronic noise, we fit a Gaussian function on our calibration data and use the $\sigma$ value in *G4Sim* to fold a Gaussian noise signal around our simulated data. This is a very simple method, and will only give us a rough estimate

[3] https://geant4.web.cern.ch/node/1619

of electronic noise in our experiment. The information about the calibration source used in the experiment is presented in table 5.1. The table shows the most presiding line in our calibration isotopes. Unfortunately, *G4Sim* does not include an energy-dependent noise signal. We can then only include an average noise disturbance over the whole energy range. For each DSSSD a Gaussian function was fitted to the main peak of each isotope in 5.1 and from this an average value was calculated. The results are shown in table 5.2. Here U3 is not included since no measurement of an $\alpha$ source directly in front of the DSSSD was made. The main point of U3 is to measure $\beta$ so this is not an issue.

| Isotope | $I_\alpha$(%) | $E_\alpha$(keV) |
|---|---|---|
| $^{239}$Pu | 73.3(8) | 5156.59(14) |
| | 15.1(8) | 5144.3(8) |
| | 11.5(8) | 5105.8(8) |
| $^{241}$Am | 85.1(3) | 5485.56(12) |
| | 13.3(7) | 5442.80(13) |
| $^{244}$Cm | 76.4(12) | 5804.77(5) |
| | 23.6(12) | 5762.16(3) |

**Table 5.1:** *The intensity and peak energy of the most dominant lines in the calibration sources used in this experiment. The data is from [31].*

The electronic noise estimates of each DSSSD from table 5.2 is included in our *Geant4* based simulation software *G4Sim*. A simulation of the $\alpha$ source as described in table 5.1 was performed on each DSSSD. That is to say, the source of the simulations was placed in

| DSSSD | U1 | U2 | U4 | U5 | U6 |
|---|---|---|---|---|---|
| $\sigma$ (keV) | 16 | 14 | 13 | 13 | 13 |

**Table 5.2:** *The electronic noise for each DSSSD where an $\alpha$ measurement was available. The $\sigma$ is extracted from a Gaussian fit to calibration data for each DSSSD. Further explanation is in the text above.*

front of each DSSSD. This is to mimic the circumstances of the experiment. An example of such simulations compared to data can be found in figure 5.1. Here we look at data from U1. From the figure we can see that the simulation fits the data fairly well, while still a bit too narrow. The two plots have been scaled for easier comparison.

## General simulation technique

The way our Monte Carlo simulation work is as follows. Generally, the information about the particles we want to simulate is drawn randomly from e.g. an energy distribution. Our simulation events are pre-generated in *Sim3a* from an energy distribution and/or angle distribution depending on the simulation of interest. Here it is important not to use the same seed for your random sampling of events when you run simulations in parallel. Perfect randomness can be difficult to obtain. We often measure something random in nature (the falling of snowflakes e.g.) and use that to generate random numbers. So the "seed" in this context is the index of the file that includes the measured "noise" you want to generate random numbers from. If you run two simulations with the same seed they will generate the same

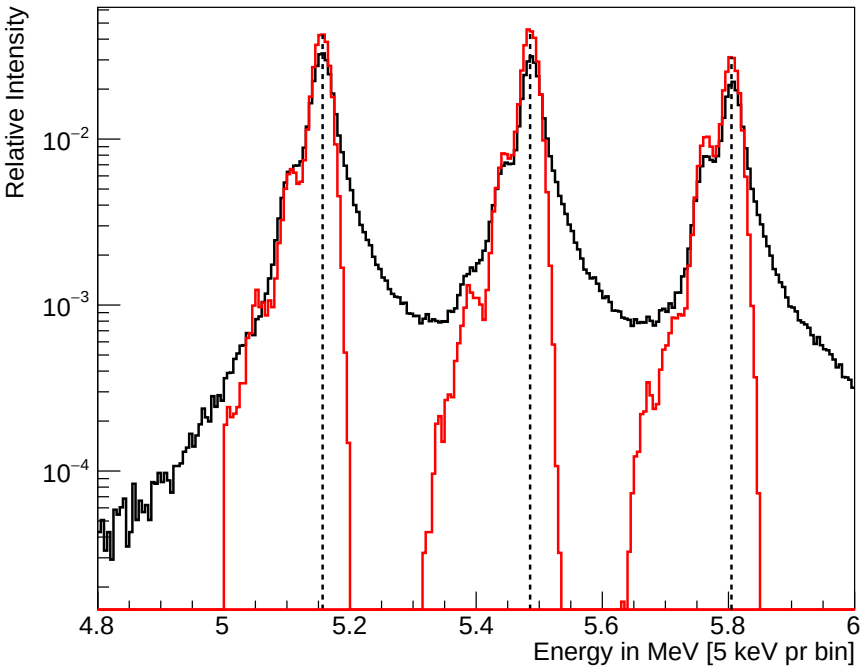


**Figure 5.1:** *Comparison between simulation (red line) of $\alpha$ source in table 5.1, and data (black line) from U1.*

"random" events and create a bias in the simulation. What kind of information the events are sampled from, is presented later in each of the simulation's sections. For each event, three $\alpha$ and one $\beta$ particle are generated. The $Q_\beta$ is determined and the $\beta\nu$ recoil is applied to the $^{12}$C nucleus. The generated data is simulated through the *G4SIM* program with the geometry shown in figure 5.2. The figure shows the 6 DSSSDs and 3 PADs as discussed in the experimental section. The

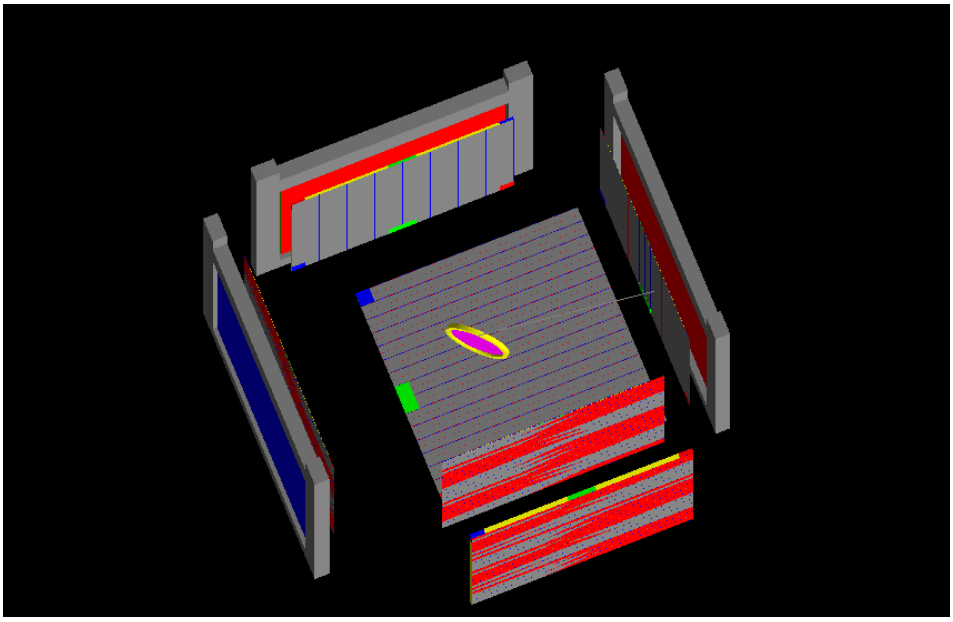

**Figure 5.2:** *Graphical visualization of the simulated geometry. Here is shown the 6 DSSSDs and 3 PADs with their frames. The target and the target holder is simulated as well.*

target and target holder are also simulated. Figure 5.2 is made with Geant4's graphical visualization tool. The beam profile is estimated from simulations of the $1^+$ state in $^{12}$C since this decay has only one decay channel (through $2^+$ states in $^8$Be based on the equation (2.2)) and has no energetically close states to create "noise" in our data (see figure 2.1). The beam profile, in this case, refers to the distribution of implantation depth and distribution of the beam size(both asumed to be Gaussian).

## 5.2 Simulations of decays through $1^+$ excitation state of $^8$Be.

We will start by simulating decays of the $1^+$ state in $^{12}$C (equation (4.5)). From the selection rules given in (2.2) we know this can only decay to the $2^+$ state in $^8$Be. The information given to the Sim3a program is:

1. –JC 1+ –JBe 2+ -L 2 –ExC 12.7MeV –ExBe 3030keV -N 200000 –seed index -o path/index.root

Where –JC is the excited state in $^{12}$C, –JBe is the excited state in $^8$Be, -L is the orbital angular momentum for $^8$Be+$\alpha$ system, –ExC and –ExBe are the excitation energy of $^{12}$C and $^8$Be, -N is the number of events to be simulated, -o is the output name and/or path and/or data type and last –seed is the index of the file used for generating random numbers as stated earlier. The index is just a placeholder for a given number. Since this is run in parallel, a different index is given for each run. We simulate 2.000.000 events. Here the specific $Q$ value is given (from the $^{12}$C excitation energy), so the information of the $\alpha$ particles is calculated from the energy and momentum restrictions of the decay. The generator from the ROOT library *TGenPhaseSpace* does this calculation. This generator calculates a weight for a given event, such that we can sample our events based on their weight to make our samples uniformly distributed in phase space. The theoretical weight is calculated with (2.6) to give the total weight as a product of the

two. When we know the maximum weight of the total weight we can use the Von Neumann method [32] of choosing the events we want to simulate. Now we are ready to run the data through G4SIM. For our first simulation the implantation depth is set to 64 nm in the target foil, and the beam has no width(the decay happens in the surface center of the foil). The simulated data is then sorted and analysed with the same method and software as described in section 4. The same scatter plot as seen in figure 4.2 is generated from the simulation and presented in figure 5.3. In figure 5.3 many of the same features from figure 4.2 is replicated. The three clusters above the main heat spot stem from $\beta$ noise. The triplet structure of this $\beta$ noise is a consequence of equation (2.6). Simulations without the weighted sampling from equation (2.6) will produce a uniformly distributed $\beta$ noise in the same place. That equation (2.6) replicates this structure is new information compared to previous work [1], where they did not simulate $\beta$ particles but rather mixed in real world data into the simulation. A thing to notice is the distribution of total momentum. The primary heat spot are located in the 0-20 MeV/c range, compared to figure 4.2 where the $1^+$ peak is near the 0-50 MeV range. This has to do with the beam profile being only located on the surface centre of the foil. Changing the beam width has the biggest impact on the angle measured, which heavily influences the momentum vectors generated from the energy and direction. To investigate the beam profile further we plot $E_{tot}$ and $P_{tot}$ (total momentum) separately in the range of 5-6 MeV. We use the energy and momentum cut from equation (4.4) and

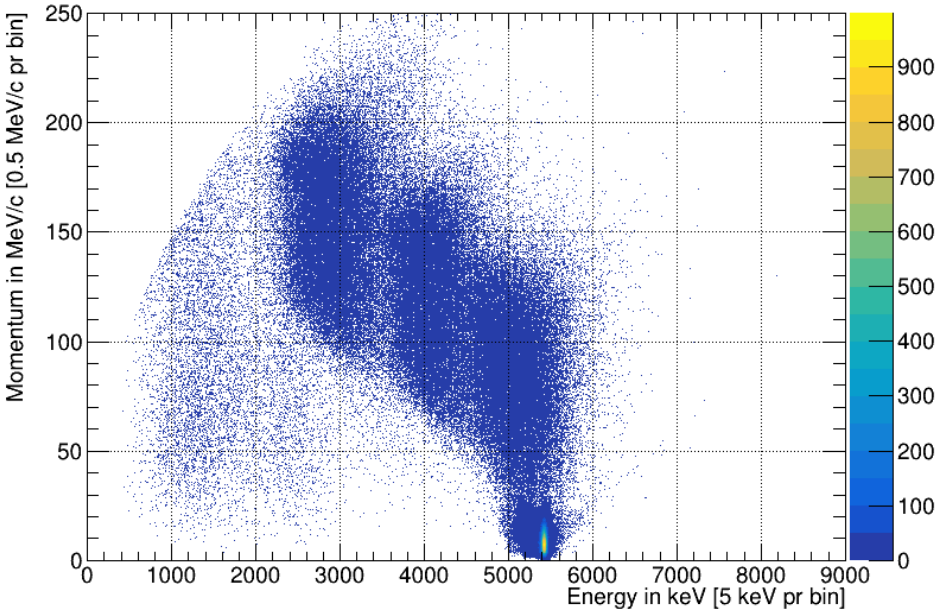


**Figure 5.3:** *Scatter plot of* $1^+$ *excited state in* $^{12}$C *simulation (equation* (4.5)*). No beam profile is added (events simulated from 64 nm implantation depth in foil surface centre).*

$E_{23} > 250$ keV. A comparison plot between data and simulation is shown in figure 5.4.

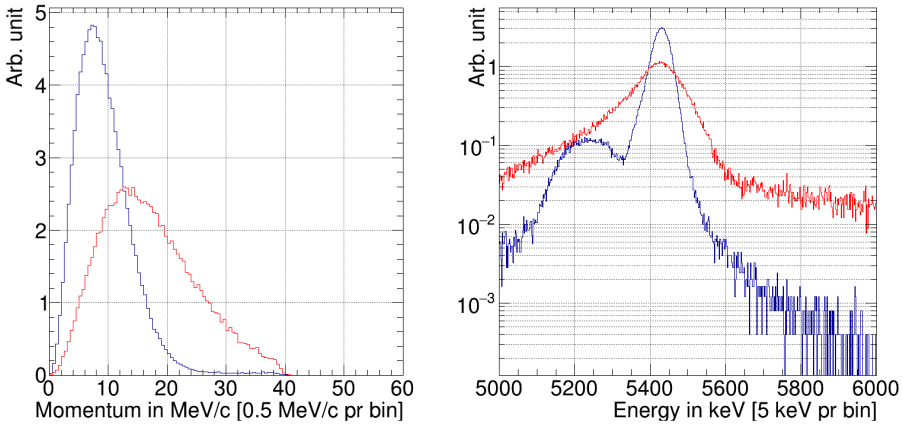


**Figure 5.4:** *Comparison of total energy(right) and total momentum (left) of the* $1^+$ *peak(data from equation* (4.5) *decay chain) between simulation (blue) and data (red). Energy and momentum cut from equation* (4.4) *as well as* $E_{23} > 250$ keV *is applied. No beam profile is added (Events simulated from 64 nm implantation depth in foil surface centre). The y-axis is of an arbitrary unit since the plots have been scaled to be more easily comparable.*

Multiple things draw attention in figure 5.4. First, if we look at the total energy spectrum (right). The main peak is located close to the same position as the data at 5429.1(5) keV which is found from a Gaussian fit to the main peak. Secondly, I specify the main peak. A satellite peak is generated below the main peak in the simulation but not in the data. This peak is due to the inclusion of the Al contacts of the DSSSD's surface. Around 3 % of the events experience a larger energy loss (since Al contacts cover 3% of the active area of our DSSSD's) than is accounted for in our energy loss corrections. That is to say, those events are energy shifted below our main peak due

to lack of correction. Besides the satellite peak, the FWHM value of the main peak in our simulation is only 23 keV. This is 18.8 % of our data peak with a FWHM of 122 keV. The satellite peak could be hidden in the data plot due to peak broadening. This would also explain the antisymmetric from of the $1^+$ data peak. In the $P_{tot}$ plot (left in figure 5.4) we see that the peak is positioned too low and is too narrow. The shape looks similar, that is, they both have a Poisson looking distribution. The question is now, *where does the broadening of energy and momentum come from?* This is where we introduce the beam profile. In our data analysis, we do not know the implantation depth of $^{12}$N. We make a qualified guess based on simulations of the stopping range of 29.1 keV $^{12}$N in carbon (figure 4.3 in [1]). So by analysing all data with an implantation depth of 64 nm we get an energy broadening from errors in our energy loss corrections. Similarly, we induce a momentum broadening by assuming the beam to have no width and that it is hitting the foil in the centre. Here the broadening arrives from errors in the direction calculations of our particles. We now try a simulation where the coordinates in the position vector of our starting point are sampled from a Gaussian distribution for each event. Our z-value (implantation depth) is sampled from a distribution around 64 nm with a $\sigma = 40$ nm. For the x,y values we sample from a Gaussian distribution around (0mm,-1mm) with $\sigma = 1.5$ mm. In the case where the value x, y or z is outside the foil (e.g. you choose a large $\sigma$ or off-set) a new value will be generated. The results of this are plotted in figure 5.5. With the added beam profile the spectral

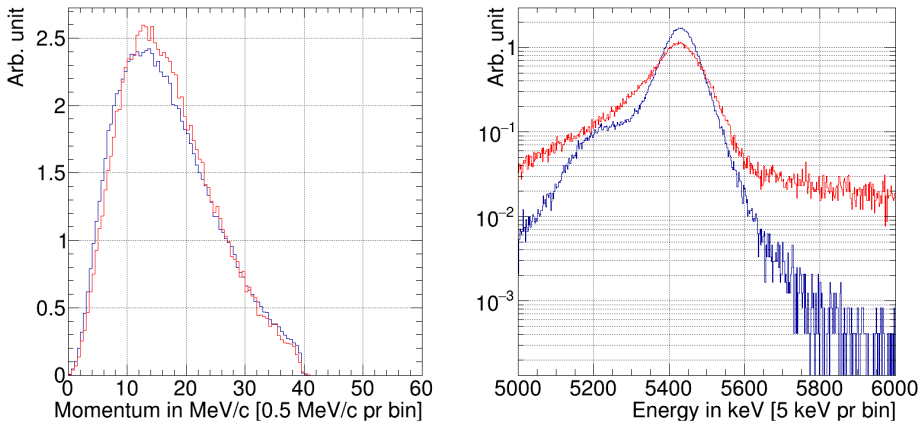


**Figure 5.5:** *Same plot as figure 5.4, but with the added beam profile as described in the text.*

comparison in figure 5.5 looks a lot better. The momentum spectrum (left) has a small offset but besides that, the shape and width of the peak are very similar. Fitting a landau function to the two momentum graphs, we found a mean peak value of 13.2(4) MeV/c with $\sigma = 5.2$ MeV/c for the simulation, compared to 14.0(5) MeV/c with $\sigma = 7$ MeV/c for data. The energy spectrum (right) has also improved significantly. While the peak position is close to unchanged (found to 5428.4(1) keV), the FWHM has increased to 42.7 keV. While still only $\approx 34\%$ of the FWHM of the data peak (122 keV), it is still an improvement. One might suggest further increasing the $\sigma$ of the implantation depth distribution. However, 40 nm is already stretching it pretty far, compared to figure 4.3 in [1], which from the looks of it suggests a $\sigma$ between 20-30 nm. From section 4.5 we suggested that

while the foil does not seem to grow linearly with each run, there does seem to be a change during the experiment. So while increasing the $\sigma$ might yield better results in terms of energy broadening, it most likely does not represent the experiment. In this work, the described beam profile will be used in future simulations. However, if time permitted it, one should have remade the simulation of $^{12}$N in carbon and used that distribution to simulate data from. From this, a more extended analysis of the foil thickness and possible alteration should be conducted. The beam profile described has been found through trial and error of many simulations. In principle, one might be able to fit the beam width and depth in the foil given enough computer power, since each simulation takes a fairly long time (5-20 min ). Such a fit would be constrained by the expected momentum and energy of a decay.

## 5.3 Simulations of decays through the $^{8}$Be ground state

In this section, we will simulate decays through the $^{8}$Be ground state. We simulate 1.000.000 events through the $0^+$ state in $^{8}$Be with an uniform energy distribution from 600 - 5000 keV total energy. Hence, the $Q$ value of our events can be between $7.8 - 12.5$ MeV, but only decays through the $0^+$ $^{8}$Be state are allowed. The reason for choosing this range is to compare $\beta$-$\alpha$ angular correlations with the results from [14]. As before we specify the settings given to *Sim3a*:

1. –JC 0+ –JBe 0+ -L 0 –ExC 12.5MeV –ExBe 0keV –seed index -o path/index.root -N 1000000

The options given here are the same as described in the previous section. Again, an analysis of the data following the same recipe from section 4 results in the scatter plot 5.6. At a first glance, the figure might not resemble the data, due to the large bright spot at the bottom of the plot. However, this can be explained by the energy range and uniformity of the used $Q$-value. Since the great bright spot in 4.2 at $E_{tot}$ between 2 and 5 MeV with $P_{tot} < 40\,\mathrm{MeV/c}$, consists of many possible transitions through the $^{8}$Be ground state, it is difficult to make a realistic simulation of this area. Nonetheless, the simulation can be used to check the $\beta$ noise above our energy and momentum cut from (4.4), as well as the $\beta$-$\alpha$ angular correlation. The $\beta$ response of the simulation seems to mimic the nature of the data.

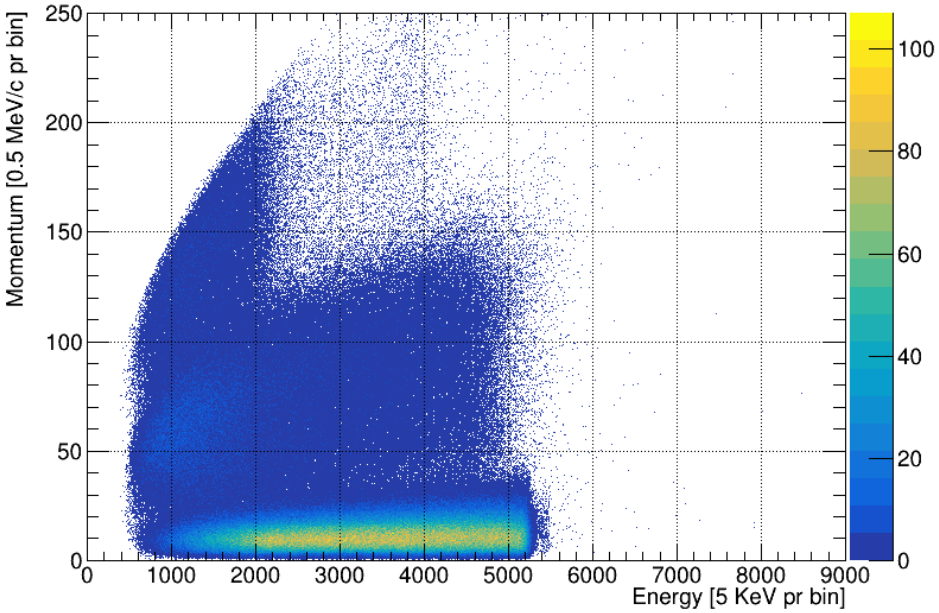


**Figure 5.6:** *Scattering plot from simulations through the* $^{8}$Be *ground state.* 1.000.000 *events are simulated, with a uniform* $Q$ *between* $7.8 - 12.5$ MeV.

Having achieved simulations of the decays through the $^{8}$Be ground state as well as the decays through the $^{8}$Be $2^{+}$ excited state, we can try to recreate the so called *Fynbo* scattering plots from 4.10. By mixing the results of both simulations, we obtain 5.7 and 5.8. The difference between these two plots is the analysis applied. In figure 5.7 the triple $\alpha$ coincidence analysis has been used, whereas the double $\alpha$ coincidence approach was applied in figure 5.8. The branching ratios have not been included, so the relative intensities of the two simulations are

not important. The point of these figures is to visualise the general structure of our simulation, which should mimic the nature of the data.

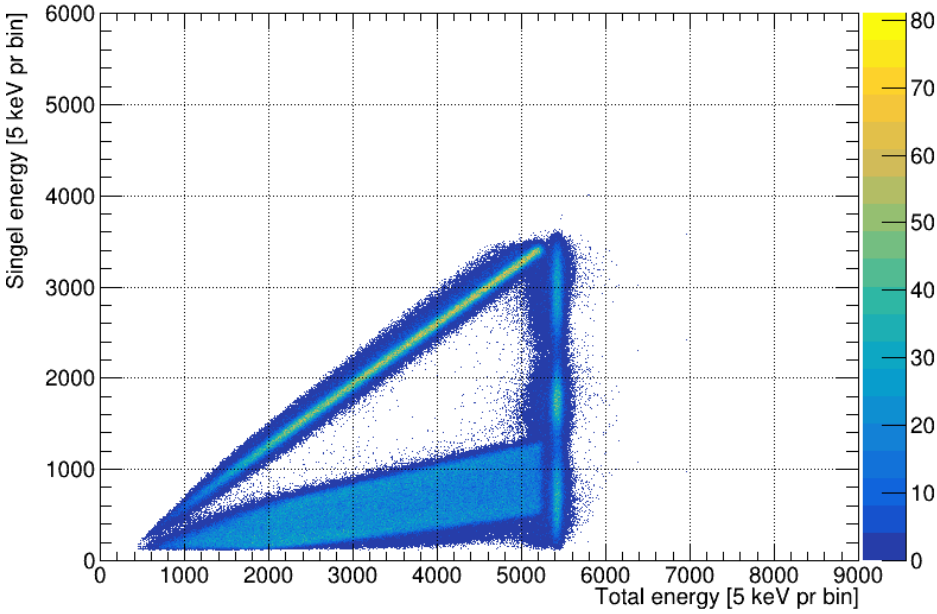


**Figure 5.7:** *Fynbo plot from simulations of decays through the ground state and* $2^+$ *state of* $^8$Be. *Triple* $\alpha$ *coincidence analysis have been used. The general Fynbo plot is described in figure 4.10.*

Generally, the two figures resemble the structure of figure 4.12 and 4.10. From figure 5.8 we see the antisymmetry of the $1^+$ peak around 5425 keV. This feature was not reproducible in section 4.7, where we tried to remove a known $\alpha$ and then reconstruct it for each event. The cause of this effect is still unknown. However, this phenomena

is reconstructed in our simulation. We also see the sharpness of the $\alpha_1$ (most energetic $\alpha$) band in the $^8$Be ground state decays. The $1^+$ peak is also more narrow in the simulation, but this we already saw in figure 5.5.

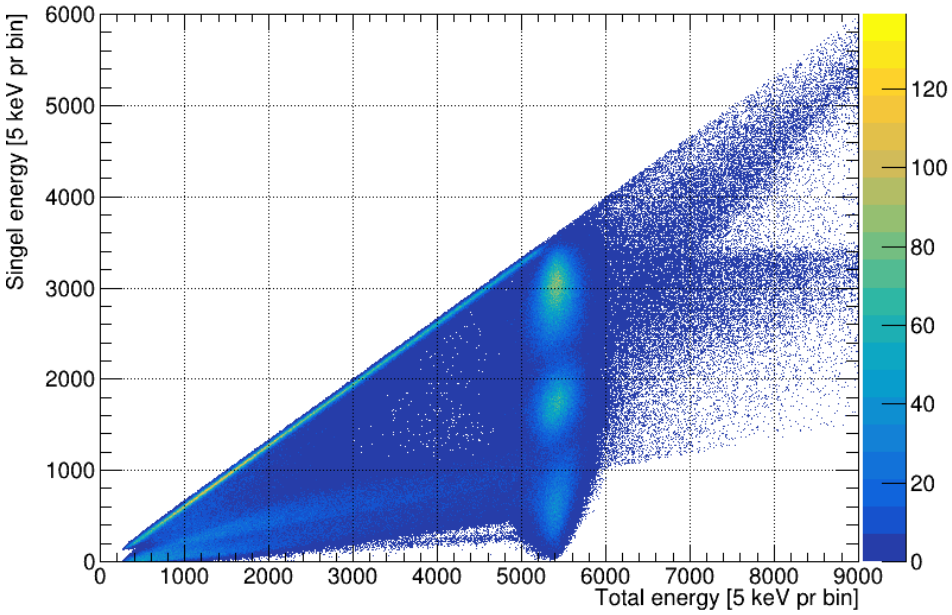


**Figure 5.8:** *Same as in figure 5.7, but with the double $\alpha$ coincidence analysis instead of triple $\alpha$.*

## 5.4 Acceptance and sensitivity

For a better understanding of the simulations, as well as how the geometry of the setup affects the analysis, we now take a look at the acceptance and sensitivity of our simulation. The acceptance refers to the percentage of the generated events that are actually detected and analysed. To know this, we must learn how many decays occur and what fraction survives the analysis. Originally a Germanium detector was present in the experiment to detect $\gamma$ radiation. The $\gamma$'s in our experiment was generated from the de-excitation of $^{12}$C. In figure 2.1, we can see that $\gamma$ decays can occur between states in $^{12}$C. Hence the detection of $\gamma$ radiation will measure how many of the different states in $^{12}$C were populated. By knowing this, we can calculate an acceptance when compared to the results of the analysis. Unfortunately, this $\gamma$ radiation detector was located too far away from the experiment, which led to noisy data. Thus, we are left with results from our simulations. We create a histogram of $E_{tot}$ for the events that we want to simulate, and another from our simulated and analysed results. A histogram of the acceptance is achieved from this by dividing the two histograms. We first take a look at our simulation through the ground state in $^{8}$Be, which is shown in figure 5.9. Here, the results from both the triple and double $\alpha$ coincidence analysis are plotted. The triple coincidence acceptance is as expected from earlier work [1]. The acceptance increases for increasing $E_{tot}$ and it converges towards $\sim 20\%$ of our generated events. Our double $\alpha$ acceptance increases faster for low $E_{tot}$ and then declines for larger $E_{tot}$ values. The reason for this

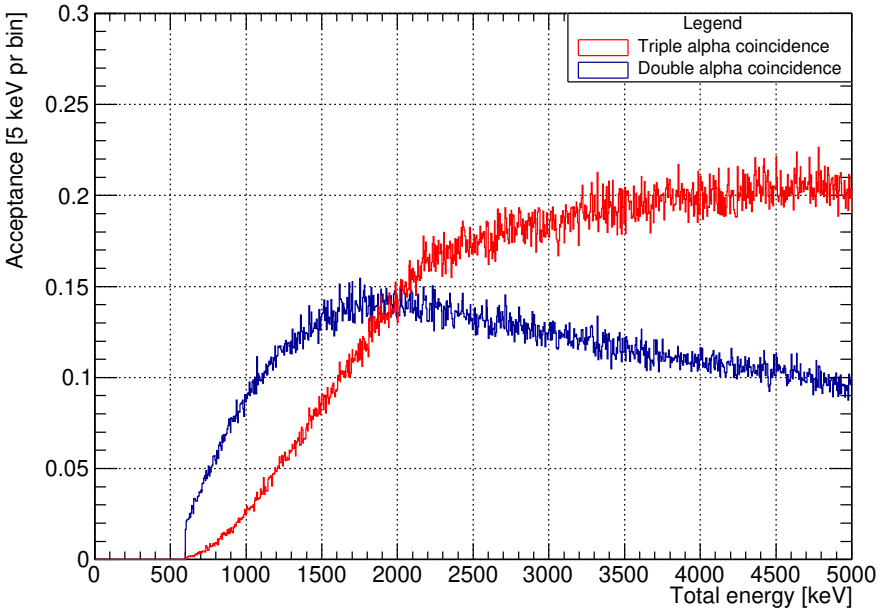


**Figure 5.9:** *Acceptance of decays through the ground state in* $^8$*Be, based on simulation from section 5.3.*

is related to the angular correlation of the three $\alpha$'s. As previously stated, due to the law of conservation of momentum, the momentum vector of $\alpha_1$ will generally be opposite that of the $\alpha_2$ and $\alpha_3$ particles, where the latter move in the same direction. So generally if we detect $\alpha_1$ we detect $\alpha_{2,3}$ in the opposite detector and vice versa. Therefore, for this particular event, we expect a greater number of detections in the triple $\alpha$ analysis as compared to the double $\alpha$ analysis. However, for $E_{tot}$ below 2000keV the $\beta$ recoil will have a greater influence, result-

ing in larger angular dispersion of the three $\alpha$ particles. This allows for the double $\alpha$ method to be more effective. For greater $E_{tot}$, this effect is diminishing and the momentum vectors of $\alpha_1$ and $\alpha_{2,3}$ become increasingly parallel. But what about decays where the $\alpha$ particles have a more uniform angular distribution? To compare with earlier work, we will perform a simulation with a uniform phase space distribution. This will give us insight into the sensitivity of decays different from the $^8$Be ground state. This simulation is performed similarly to the previous $^8$Be ground state simulation, but without using the Von Neumann sampling with weights from (2.6). The results are plotted in figure 5.10. The results for the triple $\alpha$ analysis is in agreement with previous work [1, figure 7.3]. However, the double $\alpha$ analysis yields almost double the acceptance for most values of $E_{tot}$. Not surprisingly, the acceptance is higher for the double $\alpha$ analysis. This was already hinted at in table 4.2. In many ways, figure 5.9 and 5.10 sums up the benefits of the double $\alpha$ analysis. By examining the decays where the $\alpha_1$ and $\alpha_{2,3}$ do not have a strong anti-parallel angular correlation, this analysis is very beneficial. Typically, twice the data is available this way (Three times the data if you combine the two data sets). However, for $^8$Be ground state decays, between twice and half the original data size is available dependent on the energy range. No matter what you are investigating a separate uncorrelated data set can always be regarded helpful to check for the same trends in both data sets.

The results from figure 5.10 can also be plotted as a Dalitz plot. This type of plot can more naturally present potential *dead spots* in

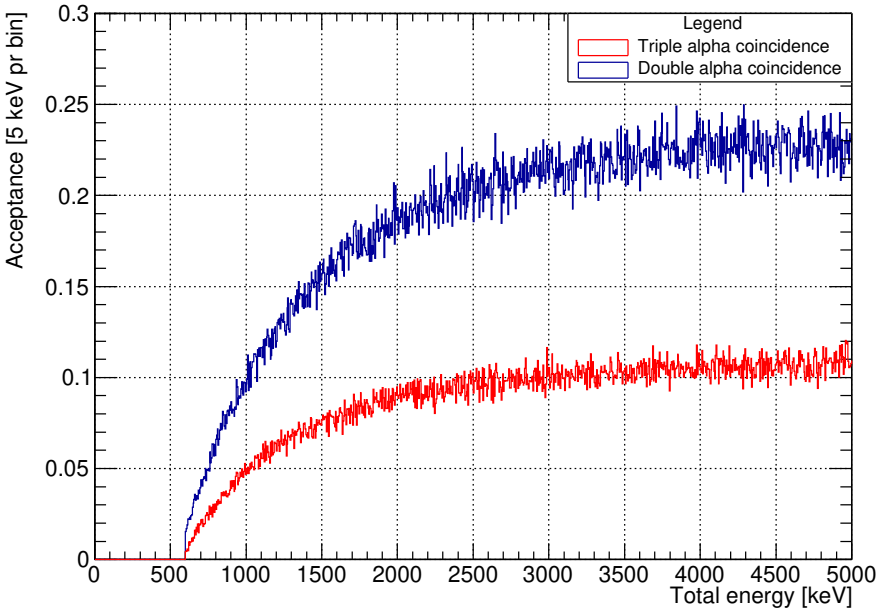


**Figure 5.10:** *Acceptance of uniform phase space decays from simulation. The red line is data analysed with the triple $\alpha$ coincidence analysis and the blue line is analysed with the double $\alpha$ coincidence analysis.*

the setup. Such spots can give information of whether some decays are unlikely to be detected in the given setup. The same energy ranges for the Dalitz plots in figure 4.15 and 4.16 are used. The results are plotted in figure 5.11 and 5.12. Events with a uniform phase space distribution give uniform Dalitz plots. In both plots, we see a cut off at the lower right and upper right corner. The lower right cut off is due to the restriction of $E_{23} > 250\,\text{keV}$. The excluded events are

primarily $E_{23} \approx 91.84\,\text{keV}$ as seen in 4.4. However, this only leads to trivial structures in our Dalitz plots as can be seen by:

$$E_1 = \frac{2}{3}(E_{tot} - E_{23}) \iff \frac{3E_1}{E_{tot}} = 2 - \frac{2E_{23}}{E_{tot}}. \tag{5.1}$$

The resulting Dalitz structure is one long line of constant $3E_1/E_{tot}$. The missing data at the upper right corner is due to the lower energy cut off, of $E > 250\,\text{keV}$. This the lowest energy we allow a particle to have in our analysis. The cut reduces the amount of data for low energy $\alpha_3$. In figure 5.11, a bright spot is shown at the tip (to the right) of the Dalitz plots for $E_{tot} > 4000\text{keV}$. These are back to back decay events. These are the events of highest $E_1$ energy and the lowest $E_{23}$ (that were not excluded by $E_{23} > 250\text{keV}$). Here the direction of $\alpha_1$ and $\alpha_{2,3}$ is close to anti-parallel, and the geometry of our setup is especially good at detecting these types of events. However, this is only for the triple $\alpha$ coincidence analysis. The double $\alpha$ data (figure 5.12) does not have this same bright spot. This is as expected. However, it does have a great bright spot at the lower right side of the plots, for $E_{tot} > 2000\text{keV}$. Generally, both plots show a uniform distribution of events. Hence, we expect to be able to detect all decay transitions with both methods. The acceptance correction that can be produced from these plots will be used to examine our data in section6.5.

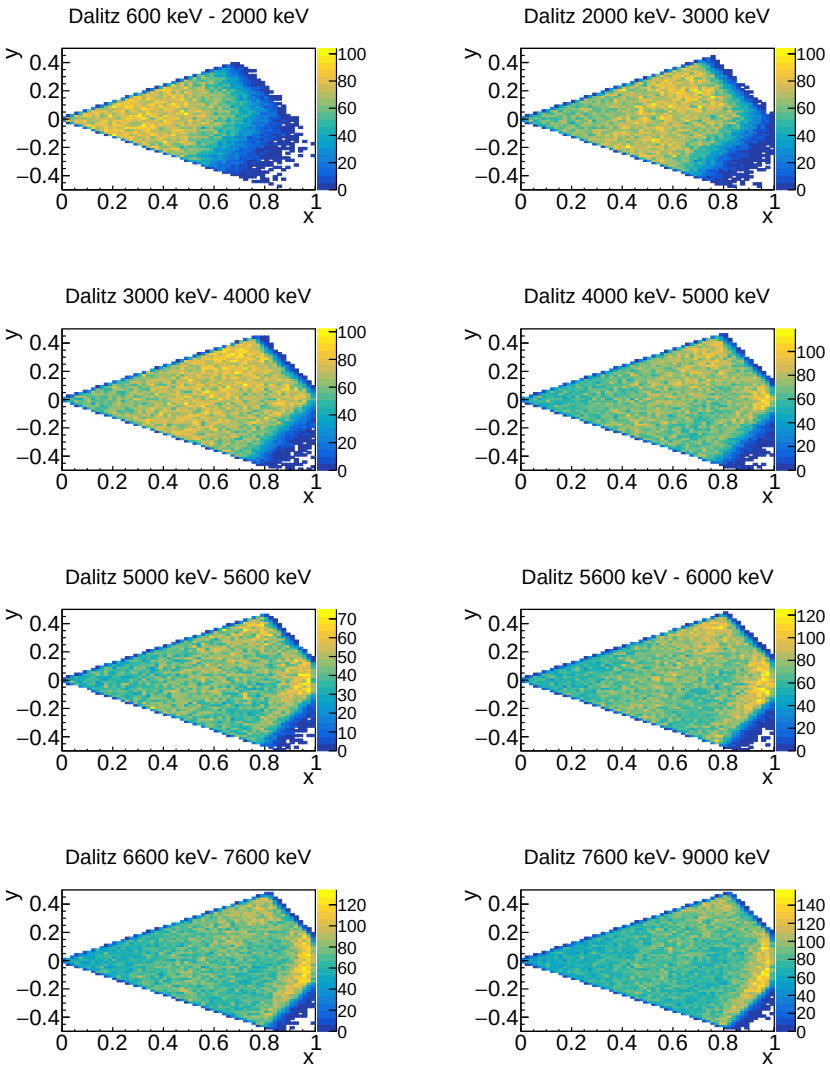


**Figure 5.11:** *Dalitz plot for the acceptance of a uniform phase space decay simulation. Data is analysed with the triple $\alpha$ coincidence analysis.*

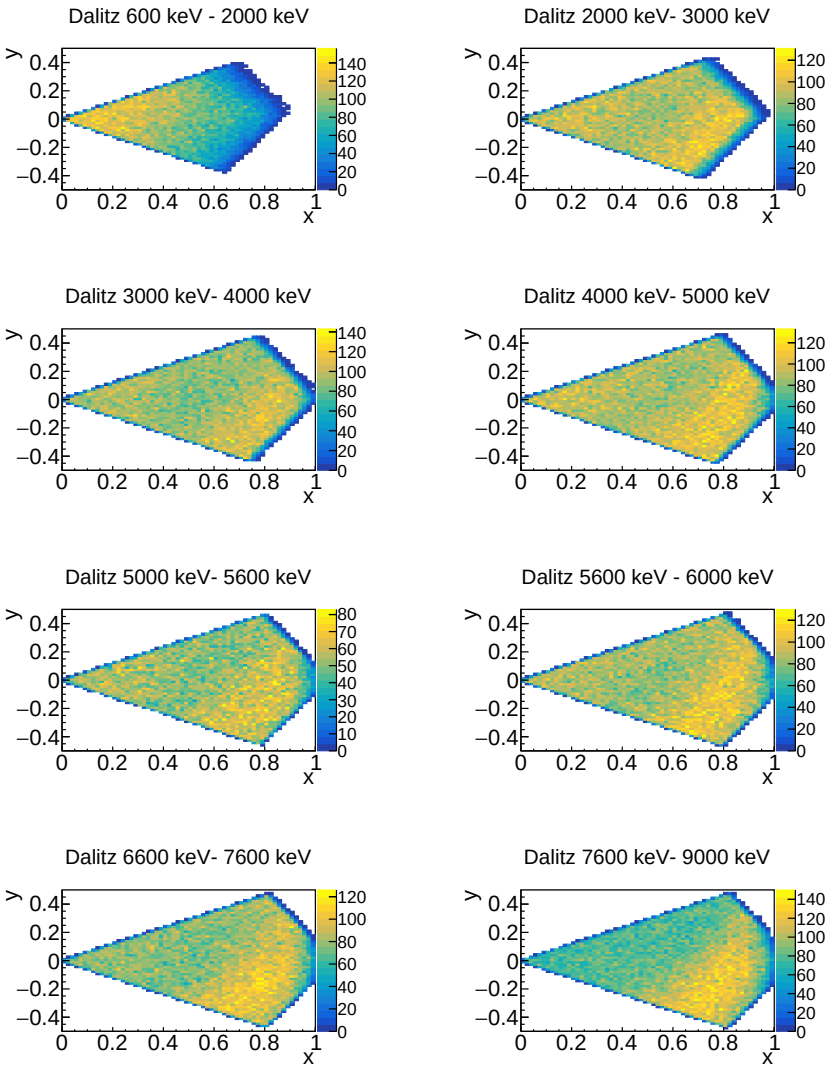


**Figure 5.12:** *Same plot as in figure 5.11 but with the double α coincidence analysis.*

# 6 Analysis and discussion

We have arrived at the last chapter of this master's thesis. Here we will investigate the angular correlation between the $\alpha_1$ and the $\beta$ particle. As mentioned in the theory section, a non-isotropic correlation could imply a second forbidden transition from the $2^+$ excited state in $^{12}$C around 9.87 MeV (See table 1.1). We will analyze the angular correlation in both the triple and double $\alpha$ coincidence analysis. The produced data sets of these two analysis methods are uncorrelated, and should therefore yield the same results. Furthermore, we will generate acceptance corrected Dalitz plots based on the simulation of uniform phase space distributed events from section 5.4.

## 6.1 $\beta$-$\alpha$ angle correlation

Our method for this analysis is as follows: The correlation implied by equation (2.10) can be used in a simple one-parameter fit proportional to the second-order Legendre polynomial. Our fitting function is then:

$$F(x_0) = 1 + A \cdot P_2(\cos(\theta)) \tag{6.1}$$

Where $A$ is our fitting parameter. The data we will be fitting is simply a histogram of the angle between the $\beta$ and $\alpha_1$ particle of our data, divided by the same histogram from our simulation. The integral of the histograms will be normalized to the same value, to make them comparable. The uncertainties here are based on the counts in each

bin of the histogram, in the familiar relation $\Delta x = \sqrt{N}$. Here N is the number of counts in bin number x. The errors undergo standard error propagation under scaling and division of histograms. The simulation uses the same beam profile found in section 5.2 and data is cut as described in each section to come. The fit is evaluated with the $\chi^2$ method, performed with ROOT's *TFitResultPtr* function.

## 6.2 Check of known isotropic $\beta$-$\alpha$ angle correlation

A general challenge in this experiment and its analysis is understanding the many decay channels that can be possible through the $^8$Be ground state. Many of which are responsible for the very broad peak in figure 4.3 between 1-4 MeV (together with the ghost peak). Hopefully, interesting physics is hidden in here. But because of the broad nature of this area, it is very difficult to test the reliability of our analysis method. Are our analysis correct or are the results obtained due to geometrical effects in our setup that we did not include? Or is there a bug in our code (hopefully not)? As we did when examining the beam profile, we turn to the $1^+$ peak (equation (4.5)). We know from equation (2.6) (and general $\beta$-decay theory), that this decay channel has an isotropic $\beta$-$\alpha_1$ angular correlation, and it is easily separated from other transitions in the data. We therefore, use this as a "baseline" test to see if we can even find isotropic $\beta$-$\alpha$ behaviour at all. We use the simulation performed in section 5.2. The data cut

used is $E_{tot} > 5300$, $E_{tot} < 5900$ and $E_{23} > 250$keV (relative energy between $\alpha_{2,3}$ as seen in figure 4.4). The uncertainty in the fit value A is scaled with $\sqrt{\chi^2/ndf}$, where $\chi^2$ is from the fit and $ndf$ is the number of degree of freedom in our fit (the binning of the histogram). It is to ensure our fit errors scale with how well the data fits the fitting equation. A more thorough explanation for this error scaling can be found in [33, section 2.5.5]. The results and the fit can be seen in figure 6.1.

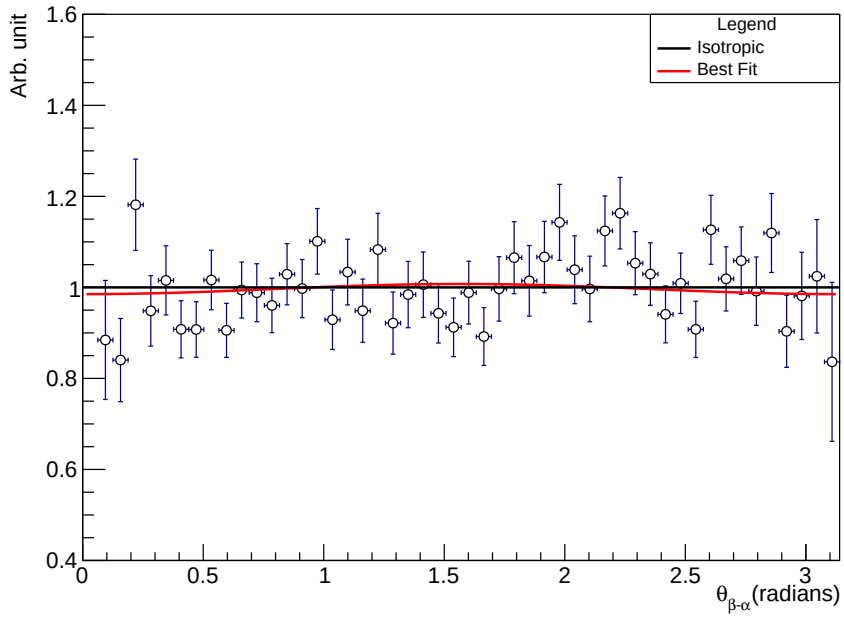


**Figure 6.1:** *Angular correlation plot of $^{12}C$ excitation energy between 12.3-12.9 Mev. The number of events from data is 14101 and 27034 from simulation. Further description can be found in the text.*

We find an $A$ value from equation (6.1) of -0.014(20), which, within uncertainties, tells us the $\beta$-$\alpha_1$ correlation is found to be isotropic for this energy range. This result adds to the certainty that we understand the theory and geometrical effects in this area. So if we find any non-isotropic signal in other energy ranges, new physics might be implied.

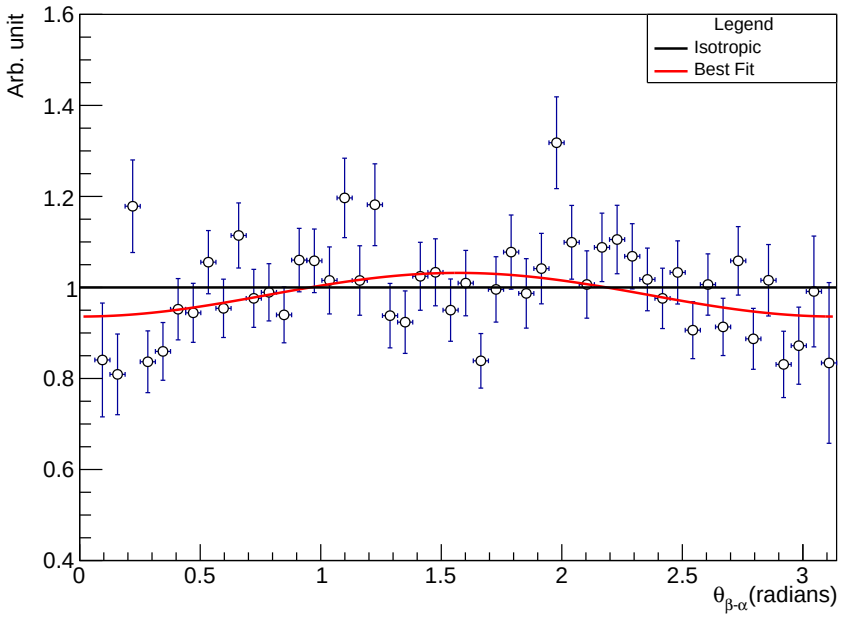


**Figure 6.2:** *Same figure as in 6.1 but without the beam profile from section 5.2.*

The fit dependency of the x,y coordinates of the beam profile (the beams width and offset on the foil surface) can be roughly estimated by removing the beam profile implemented in section 5.2. The resulting

fit can be seen in figure 6.2. We find a fit coefficient of $A = -0.063(19)$. So now the $1^+$ peak data does not have an isotropic signal. It is tempting to conclude that we got it right by including the beam profile, and from this, we can trust any future non-isotropic signal that we may find. However, we estimated a beam width of 1.5 mm and an offset of -1 mm based on the "smearing" in $P_{tot}$. This smearing could perhaps have been achieved by another choice of x,y. That is to say, we might just have found one of the multiple-beam profiles to fit the $P_{tot}$ peak signature. Due to time restrictions, no further analysis on this will be performed in this work, but this should be done in future work. We do conclude, however, that the inclusion of the beam profile had a positive impact on our fit, and made the fit of the $1^+$ peak isotropic as it should be. We continue our $\alpha_1$-$\beta$ correlation examination onto the $^8$Be ground state decays.

## 6.3 $\beta$-$\alpha$ Angular correlation of reactions through the $^8$Be ground state

We use the same simulation as conducted in section 5.3. As previously we calculate the angle between the $\alpha_1$ and the $\beta$ particle. We use the momentum and energy cut from equation (4.4) and $E_{23} < 250$. In principle, the potential $2^+$ state above the Hoyle state in $^{12}$C, could decay to the $2^+$ state of $^8$Be. But since this would require a more complex simulation we only investigate signals to the ground state of $^8$Be. Different from the previous fit we now want to examine a variety

of energy ranges. We divide our data into 500 keV $^{12}$C excitation energy ($\mathrm{Ex}_C$) ranges. That is to say we make an angular fit with equation (6.1) on data between $\mathrm{Ex}_C$ 9-9.5 MeV, 9.5-10 Mev etc. An example of the scaled histograms of $\alpha_1$-$\beta$ angular correlation from the simulation and data can be found in figure 6.3. This is for $\mathrm{Ex}_C$ between 10-10.5 MeV. Similar to the last section we use $\chi^2$ statistics. The fit value for all the $\mathrm{Ex}_C$ ranges can be seen in figure 6.4, together with a comparison of the fit values obtained in [14].

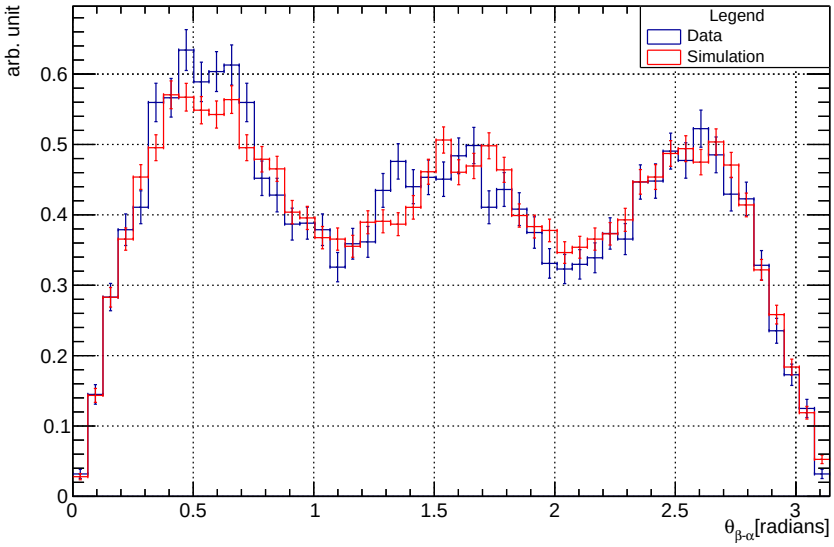


**Figure 6.3:** *Histograms of the angular distribution between $\alpha_1$ and $\beta$ for $^8$Be ground state decays, between 10-10.5 MeV $^{12}$C excitation energy. The histograms have been scaled to have the same integral. The simulation is described in section 5.3.*

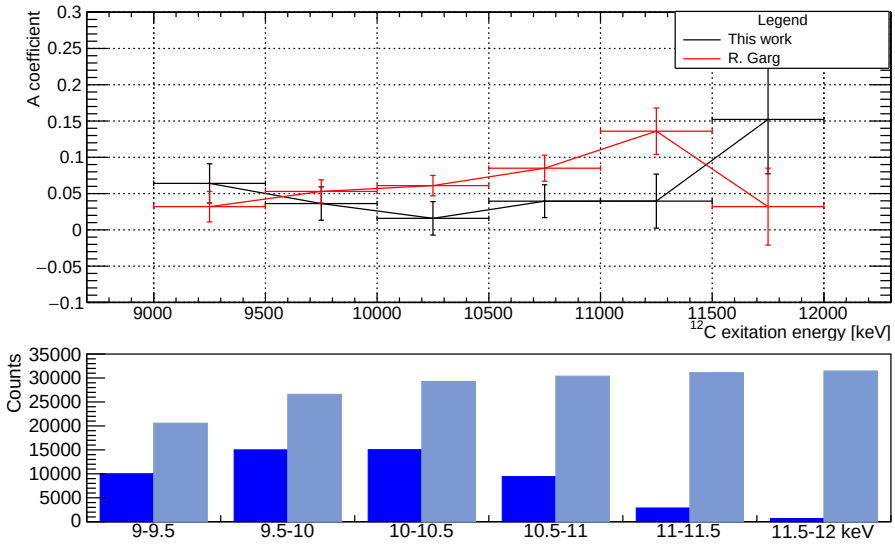


**Figure 6.4:** *(Upper plot) Fit values from $\alpha_1$-$\beta$ angular correlation fits for different $^{12}C$ excitation energy ($Ex_C$) ranges. The simulation used is described in section 5.3. The error in the x-direction indicates the $Ex_C$ range used. (Lower plot) The amount of data available for each fit. Here the dark blue is experimental data, and the light blue is the simulation.*

The fit results plotted in figure 6.4 is also printed in table 6.1. In short, all the fit values are different from an isotropic $\alpha_1$-$\beta$ distribution, except from $\mathrm{Ex}_C$ between 10-10.5 Mev. It is worth noticing that besides the fit values being different from 0, some of them are quite a bit away from zero. Where the furthest is A = 0.15(6). Now we examine what the fit coefficient actually represents a bit more deeply.

You can write it as:

$$A = \sum_i b_i \times A*_i \tag{6.2}$$

Here $A*_i$ is the anisotropy of a decay mode, with relative strength $b_i$ ($b_i$ can have values between 0 and 1). In [14], most of the anisotropy is suggested to arrive from the $2^+$ state in $^{12}$C. This would place the anisotropy in the order of $10^{-1}$ (given one decay mode mainly contributes to A), which for the $2^+$ state is two orders of magnitude larger than the theoretical value of $0.64 \times 10^{-3}$ [24]. It is of course tempting to discard this measurement since not much data is available in this area ($\approx$ 600 events), but it is still of interest. We should also note that any fit value around 0.06 could still be isotropic since we in the previous section found that the beam profile alone was able to move the fit value 0.05. The earlier work by R. Garg [14], is drawn in as a red line in figure 6.4. As seen in the figure we were not able to replicate the findings in this work. While we also find a non-isotropic signal, the graphs don't agree on the strengths of these signals and their relation to the $^{12}$C nuclear excitation energy. This means either that there are some disagreements in the data reduction method, simulation method, geometrical or detector/setup corrections (detector/setup corrections is energy loss, detector response, etc.). In our setup, we have two DSSSDs to measure $\beta$ particles. Namely U4 and U3. The way we differentiate between particles in these is different. In U4 we mark a hit as a possible $\beta$ if a signal is also detected in the PAD P4 behind it. Else we mark it as an $\alpha$. With hits in U3, we

always mark them as $\beta$'s since we expect any $\alpha$ particles to be stopped in U2 in front of U3. This might give some bias in the $\beta$'s detected since we can see very different fits for the data from U4 and U3. Two similar fits as in figure 6.4 have been made, but for $\beta$'s only detected in U4 and another for U3. This can be seen in figure 6.5 and 6.6. Here we see that the data from U3 gives a very isotropic signal over the whole energy range, while the U4 fit gives, a more non-isotropic signal for lower energy but otherwise agrees (not including the 11.5-12 MeV). Here we remember that our fits are dependent on our simulation. So does our simulation have a bias against one or the other detector? There is no big difference in the amount of data detected in the two DSSSDs. We observe a difference between simulation and data of 0-15 %. If there is any difference it should be in what kinds of $\beta$ particles they detect. By looking at figure 5.2 we also note that the U3 does not have a frame programmed. Backscattering electrons from the frame might be of importance here as well. Since the U3 has a simpler way of detecting $\beta$ particles, this should be the more trusted detector of the two. The data from this detector yields no sign of a non-isotropic signal. Unfortunately, due to time restrictions, this will not be investigated further.

| $Ex_C$ | 9-9.5 | 9.5-10 | 10-10-5 | 10.5-11 | 11-11.5 | 11.5-12 |
|---|---|---|---|---|---|---|
| $A$ | 0.064(27) | 0.036(22) | 0.015(23) | 0.039(22) | 0.039(37) | 0.152(75) |

**Table 6.1:** *Fitting values from figure 6.4. $Ex_C$ is excitation energy for $^{12}C$ in* MeV. *The fitting function used* (6.1).

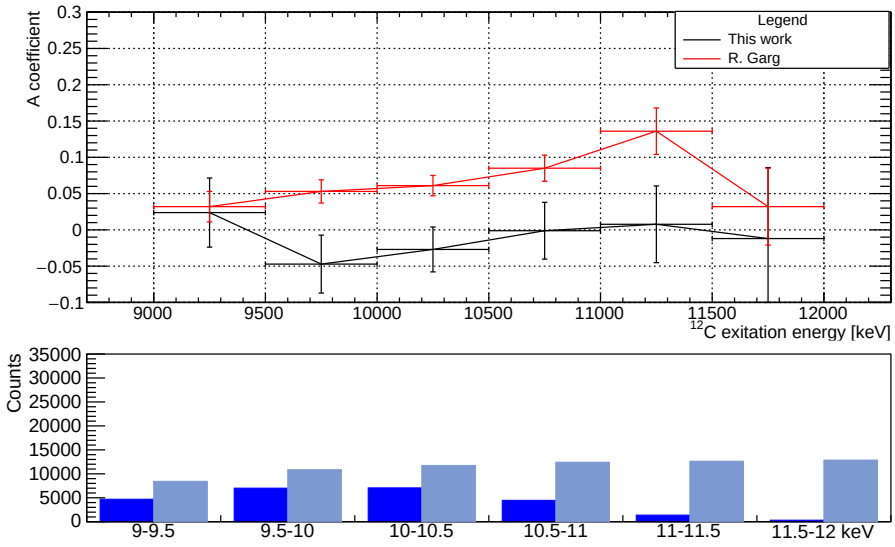


**Figure 6.5:** *Same figure as in 4.11 but only for $\beta$ particles detected in U3.*

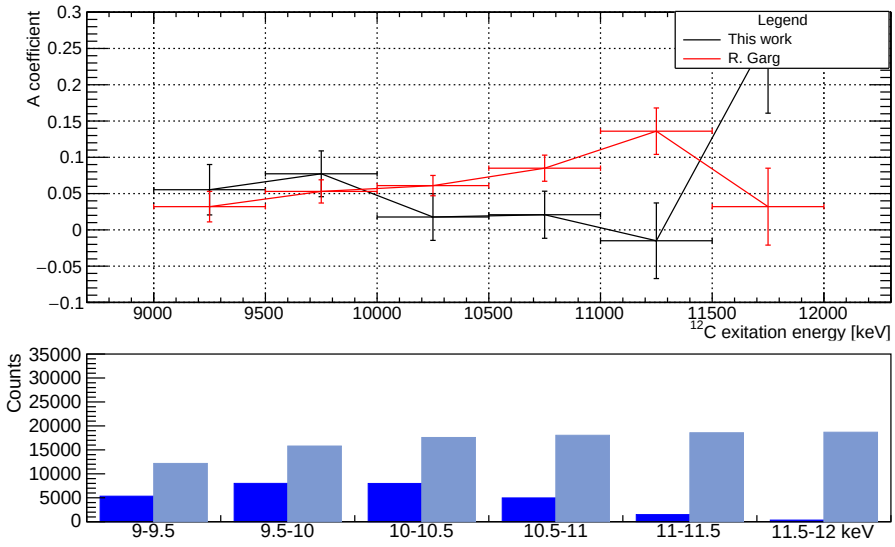


**Figure 6.6:** *Same figure as in 4.11 but only for $\beta$ particles detected in U4.*

## 6.4 $\beta$-$\alpha$ angle correlation Double-$\alpha$ events.

In figure 5.9, we saw that the double $\alpha$ coincidence analysis was less effective for decay to the $^8$Be ground state, for most of the energy range. We still, however, check to see if any relevant information could appear from a $\alpha_1$-$\beta$ angular analysis as in the last section. We can not approach this analysis with the same method as in section 4.4, since we now have to include events with three hits. Hopefully two $\alpha$ and one $\beta$ particle. We make use of the relative energy of the two

low energy $\alpha$'s namely $\alpha_{23}$. As calculated in figure 4.4, we expect the relative energy for $^{8}$Be ground state decays to be around 91.84 keV. For events with three hits, we then try every combination to find the particle pair with the lowest relative energy. With this approach, we find 27000 events, which is about half the events found in figure 6.4. Here $\approx 66\%$ of them are located in U5. This is not strange since as previously stated $\alpha_1$ and $\alpha_{23}$ have close to an anti-parallel trajectory for the $^{8}$Be ground state decay, and we do not have a detector above our set up. So all the $\alpha_{23}$ detected in U5 would have their $\alpha_1$ in the top of the setup where no DSSSD is placed. The simulation does unfortunately not replicate data in a good enough way for a fit to be possible. Since the simulation is that much off, the fit will always give a value far away from 0, with great uncertainties (Since equation (6.1) does not fit data very well). It was therefore determined that the double $\alpha$ analysis would not benefit this $\alpha$-$\beta$ angular analysis in any useful way.

## 6.5 Acceptance corrected Dalitz plots.

As mentioned in section 4, we will now revisit our Dalitz plots (figure 4.15 and 4.16) and try to apply an acceptance correction to them. The ideal way to do this is to simulate all the possible events and weigh them accordingly to their branching ratios. We can then simply divide the Dalitz plot of the events we want to simulate with the simulated and analysed events. This plot tells us how many of the different

decays survived. Hence you can use that to correct your data. Of course, if we could do it this way, there would be no reason to do the experiment in the first place since we already have the information of interest. What we do instead is use the simulation of $\alpha$ particles uniformly distributed in phase space from figure 5.12 and 5.11 to generate an acceptance Dalitz plot from this, as described prior. The resulting acceptance corrected plots are presented in figure 6.7 and 6.8. These figures will be involved in a more qualitative discussion of the possible decay modes that could have produced these plots. More extensive Dalitz plot fits is needed to be able to conclude further, similar to what was done in the earlier work [1]. Due to time restrictions, this was not done here. in figure 6.7 we note that the few yellow points in the plots 600-5000 keV, are an error from the acceptance correction. If we expect very few points in an area, and we find some anyway they get blown out of proportion since we divide the bin with a very small number. The z-scale have been adjusted so it is easier to see structures in the plot itself. Qualitatively what we can see is an agreement between the two plots at 2000-3000 keV, 3000-4000 keV and 5000-5600 keV. The 600-2000 keV plots seem to disagree. Where the triple $\alpha$ analysis gives a more uniform plot, the double $\alpha$ analysis gives something different from uniform. The shape of the plot does not resemble any of the theoretical estimations from figure 2.3 and 2.4. More examination is needed here. In the 4000-5000 keV range we have the same bright spot in the upper right corner in both plots, but the triple $\alpha$ data also have a spot on the left tip. This could be

a combination of a (2,2,2) and a (2,2,0) from figure 2.3 and 2.4. But interestingly enough we do not see this in the double $\alpha$ plot. In the 5000-5600 keV range a very clear $1^+$ peak is seen. This peak, however, is also seen in the 5600-6000 keV range for the double $\alpha$ plots. This is because of the energy broadening of the double $\alpha$ analysis. So this range is difficult to compare. The 6600-7600 keV and 7600 - 9000 keV ranges are where the double $\alpha$ analysis is most beneficial. The structure of the 6600-7600 keV range between the double and triple $\alpha$ plots agrees well, but with simply more data in the double $\alpha$ plot. The same structure is seen in the 7600 - 9000 keV range for double $\alpha$. This could resemble a (2,4,2) decay together with a (2,2,2) or (2,0,2) decay. While this more qualitative approach can give some intuition of the two analysis methods, a more quantitative method is very much needed. We do expect that the two methods should give the same Dalitz plots after acceptance correction, and with only a qualitative comparison it is difficult to tell how much they disagree and where. Similarly, instead of estimating the possible decay modes that could give rise to these plots, it would be much better to simulate the decay modes, run them through the two analysis methods and then fit the different decay modes to the observed plots. Time restrictions, unfortunately, deny us of this possibility.

## 6.6 Improvement for future experiments/analysis

In this section we take a look at how to improve the experiment and the analysis in future work. The $\alpha$-$\beta$ angular studies from section 6.2 indicated a strong influence from geometrical effects. This highlights the importance of momentum measurements in our setup. A greater pixel resolution in our DSSSDs together with beam width measurements would therefore be beneficial. This will also improve the double $\alpha$ analysis, since it depends on conservation of momentum for reconstructing the third $\alpha$. However, charge sharing/summing will become an increasing problem with higher pixel density. While $\alpha$-$\beta$ angular studies rely more on beam width estimations, double $\alpha$ analysis also greatly benefits from a better understanding of beam implantation depth. While a foil thickness of 100nm is a good choice for stopping $^{14}$N with 29.1MeV, the understanding of foil changes during the experiment should be improved. This could be done with more frequent measurements of the foil thickness during the experiment. Besides experimental improvements, the R-matrix fits of the newly acquired data from double $\alpha$ coincidence analysis should be performed. Especially in the higher $^{12}$C excitation energy regime.

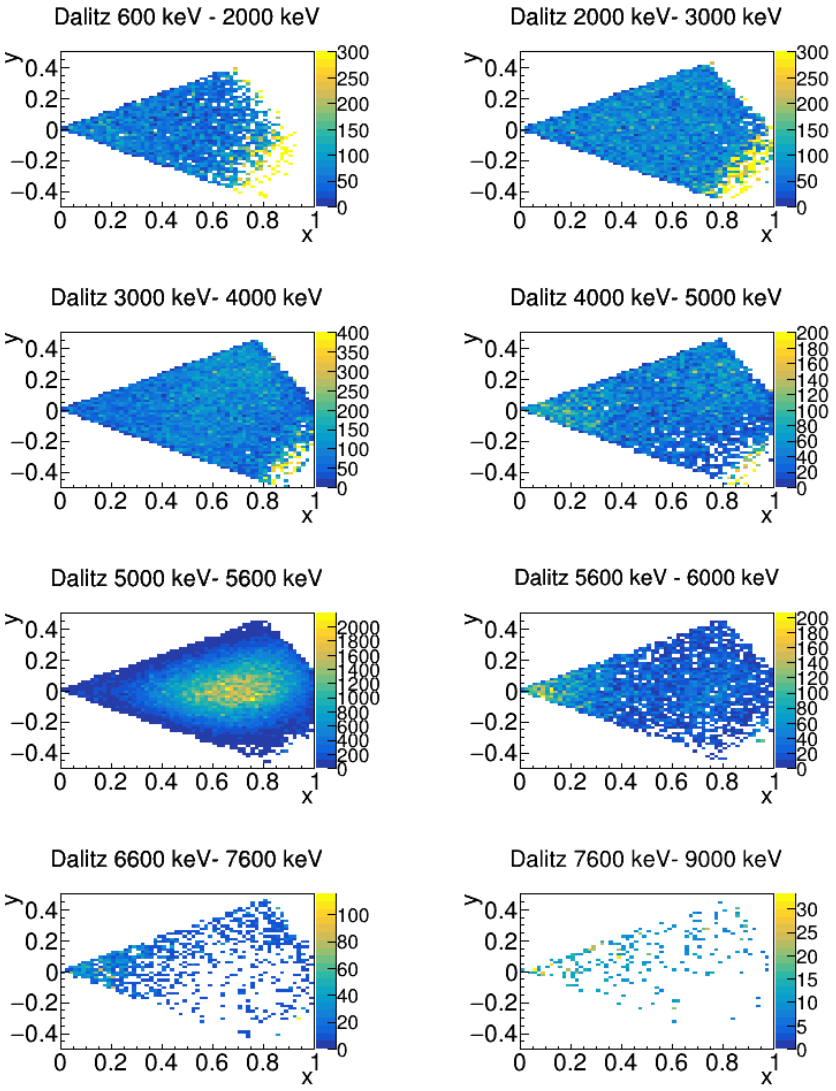


**Figure 6.7:** *Acceptance corrected Dalitz plots from triple α coincidence analysis.*

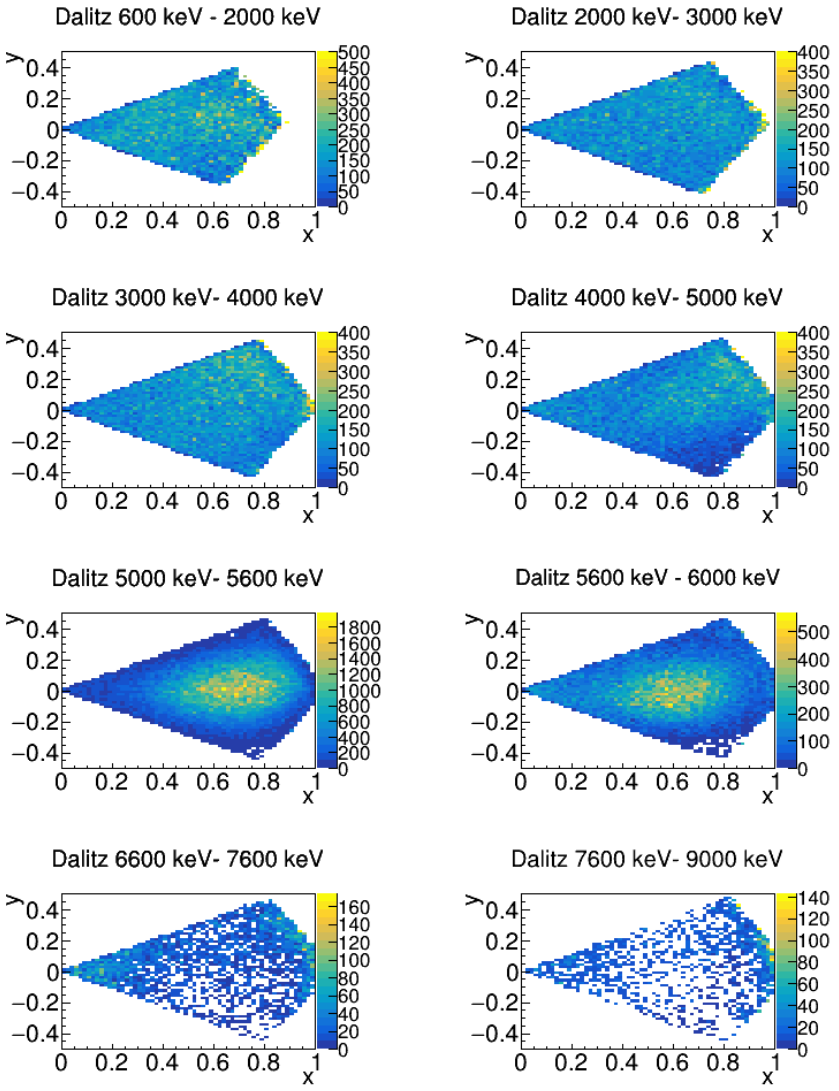


**Figure 6.8:** *Acceptance corrected Dalitz plots from double $\alpha$ coincidence analysis.*

## 6.7 Summary

In this master thesis, we extended the analysis of earlier work [1] by including double $\alpha$ coincidence analysis, *Geant4* simulations and $\alpha$-$\beta$ angular studies. Many of the main spectra from the earlier work were verified in this independent analysis, which is best seen by comparing the main spectra such as figure 4.10, 4.2 and 4.15 to the corresponding figures in [1]. The purpose of the double $\alpha$ coincidence analysis was to test in which cases such analysis was beneficial. This can mainly be seen in the acceptance plots of figure 5.9 and 5.10. Here the acceptance of the method was tested against simulations of uniform phase space distributions and of $^{8}$Be ground state decays from reaction (2.1). These plots show that the main benefit of this analysis lies in the energy spectrum ($^{12}$C excitation energies $>$ 5 MeV). Here about twice the data could be found, compared to the original triple $\alpha$ coincidence analysis. The benefits of this can especially be seen in figure 6.8, where signs of $^{12}$C($2^+$) $\rightarrow^{8}$ Be($2^+$) can be found in 7.6-9 MeV $^{12}$C excitation energy region. The *Geant4* simulations yielded interesting results in regards to $\beta$ signals and estimations of the beam profile. The $\beta$ noise signal seen in figure 4.2 was replicated in the simulation. The beam profile was estimated as a Gaussian distribution with $\sigma_{x,y} = 1.5$mm, around (0 mm, -1mm) center. The depth of the beam in the target foil was estimated to $\sigma_z = 40$ nm around 64 nm peak value. A comparison between the simulation and data of the $1^+$ peak (equation (4.5)) in figure 5.4 and 5.5, shows a good agreement in $P_{tot}$ but less in $E_{tot}$. This is most likely due to changes in the target foil thickness and structure

during the experiment. In earlier work [1] the foil was thought to be growing in thickness. However by examining the $1^+$ peak position with a fixed and a linearly increasing thickness for increasing measurement number (e.g. 1 is the first measurement and 100 is the last measurement), we found little tendencies for a linearly increasing foil thickness. The result of the two analysis methods is illustrated in figure 4.8 and 4.9. However, even though the foil thickness did not seem to increase linearly, missing information about the foil and its change during the experiment could explain the missing $E_{tot}$ broadening of the $1^+$ peak between the simulations and data. The examination of the $\alpha$-$\beta$ angular correlation was motivated by earlier results from Ph.D. R. Garg [14], in which a non-isotropic signal was found for $^{12}$C excitation energies between 9-11.5 MeV. This behavior was explained to arise from first forbidden decay $1^-$ and second forbidden decays from the $2^+$ state in $^{12}$C and should be proportional to the second-order Legendre polynomial. A fit of such a relation (equation (6.1)) was tested on data. While a non-isotropic signal was found, the values and energy relation were not reproduced. A comparison of the fitted values of this work and R. Garg can be found in figure 6.4. The $\alpha$-$\beta$ angular relation was also tested on the $1^+$ peak (equation (4.5)), where the expected isotropic behavior (fit value A = -0.014(20)) was only found if a suitable beam profile was included in the simulation. Otherwise, the fit yielded A = 0.063(19). That is to say, any signal around 0.063 could be explained by potential systematic errors. Furthermore, if we separated our data into events where the $\beta$ particles were detected in

U3 and U4 respectively, we obtained different fit results. The U3 data set gave an isotropic signal over the entire energy range, while the U4 data gave a non-isotropic signal between 9-10 MeV and 11.5-12 MeV. The data from U3 should be more trustworthy since it is easier to differentiate between $\alpha$ and $\beta$ particles compared to U4. The spread in the current results indicates that systematic errors are present and that it is too early to conclude if forbidden decays are present or not.

In conclusion, the double $\alpha$ coincidence analysis produced an additional useful data set. The data output was significant for the higher and lower excitation energies for $^{12}$C, where data was lacking from the triple $\alpha$ coincidence analysis. *Geant4* simulations were very useful in the determination of geometrical effects from our detector setup and beam profile. These effects were estimated to have a sizable effect on our $\alpha$-$\beta$ angular studies, to a degree that it is not possible currently to conclude if any forbidden decays are present in our data.

# Appendix

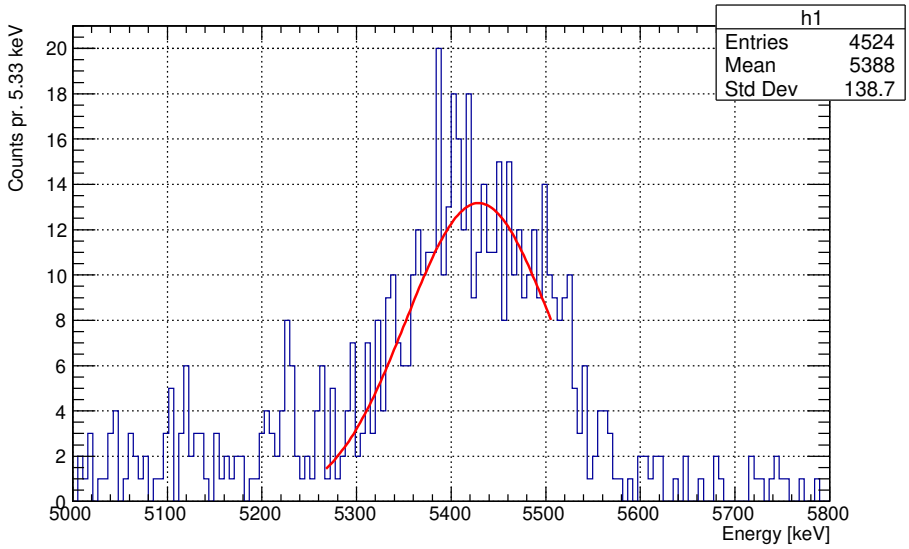


**Figure 6.9:** *Gaussian fit of triple $\alpha$ coincidence analysis. The fitted peak arise from the* (4.5) *decay.*

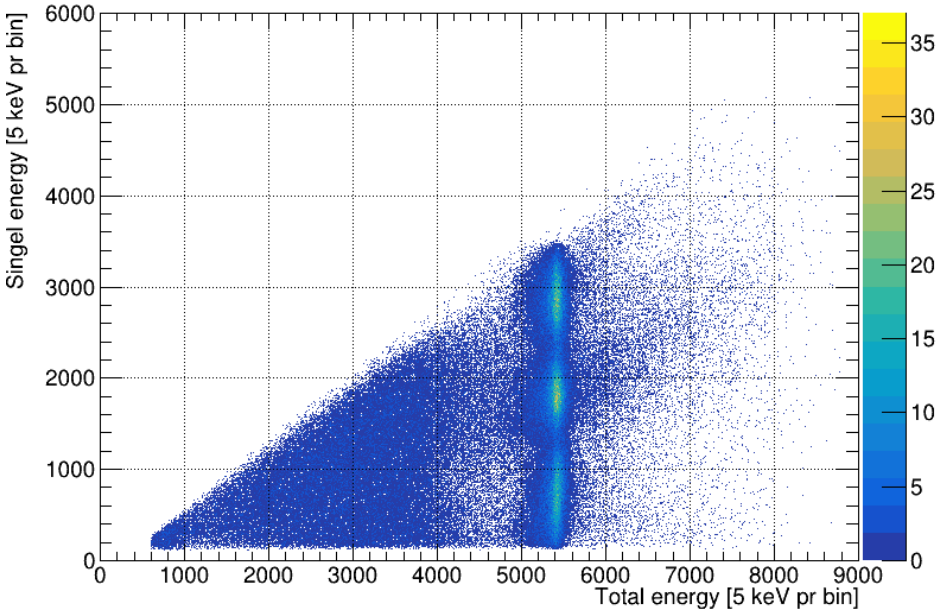


**Figure 6.10:** Fynbo *scattering plot from triple $\alpha$ coincidence analysis. $E_{23} > 250$keV (relative energy of $\alpha_2$ and $\alpha_3$ ) has been applied to isolate decays from* (4.5).

# Bibliography


[1] J. Refsgaard, *RESONANCES , R-MATRIX–ROTATIONS IN* $^{12}C$ *?* PhD thesis, Aarhus University, 2016.

[2] A. Gad, *Deciphering Resonances in* $^{12}C$ *- A* $\beta$*-decay study of* $^{8}Be$. PhD thesis, Aarhus University, 2021.

[3] E. M. Burbidge, G. R. Burbidge, W. A. Fowler, and F. Hoyle, "Synthesis of the elements in stars," *Rev. Mod. Phys.*, vol. 29, pp. 547–650, Oct 1957.

[4] E. E. Salpeter, "Nuclear Reactions in Stars Without Hydrogen.," *apj*, vol. 115, pp. 326–328, Mar. 1952.

[5] E. J. Öpik, "Stellar models with variable composition. ii. sequences of models with energy generation proportional to the fifteenth power of temperature," *Proceedings of the Royal Irish Academy. Section A: Mathematical and Physical Sciences*, vol. 54, pp. 49–77, 1951.

[6] H. Kragh, "An anthropic myth: Fred hoyle's carbon-12 resonance level," *Archive for History of Exact Sciences*, vol. 64, pp. 721–751, 11 2010.

[7] F. Hoyle, D. N.F.Dunbar, W. Wenzel, and W. Whaling, "A state in $c^12$ predicted by astrophysical evidence," *Phys. Rev.*, vol. 92, p. 1095, 01 1953.

[8] D. N. F. Dunbar, R. E. Pixley, W. A. Wenzel, and W. Whaling, "The 7.68-mev state in $c^{12}$," *Phys. Rev.*, vol. 92, pp. 649–650, Nov 1953.

[9] C. W. Cook, W. A. Fowler, C. C. Lauritsen, and T. Lauritsen, "$b^{12}$, $c^{12}$, and the red giants," *Phys. Rev.*, vol. 107, pp. 508–515, Jul 1957.

[10] C. W. Cook, W. A. Fowler, C. C. Lauritsen, and T. Lauritsen, "High-energy alpha particles from $b^{12}$," *Phys. Rev.*, vol. 111, pp. 567–571, Jul 1958.

[11] F. Barker and P. Treacy, "Nuclear levels near thresholds," *Nuclear Physics*, vol. 38, pp. 33–49, 1962.

[12] J. Kelley, J. Purcell, and C. Sheu, "Energy levels of light nuclei a=12," *Nuclear Physics A*, vol. 968, pp. 71–253, 2017.

[13] A. M. Lane and R. G. Thomas, "R-matrix theory of nuclear reactions," *Rev. Mod. Phys.*, vol. 30, pp. 257–353, Apr 1958.

[14] R. Garg, *Hoyle state rotational excitation studied via $\beta$-triple-$\alpha$ angular correlations*. PhD thesis, University of York, 2017.

[15] F. Ajzenberg-Selove, "Energy levels of light nuclei a = 11−12," *Nuclear Physics A*, vol. 506, no. 1, pp. 1–158, 1990.

[16] S. Wong, *Introductory Nuclear Physics*. John Wiley & Sons, 11 1998.

[17] R. Dalitz, "Cxii. on the analysis of $\tau$-meson data and the nature of the $\tau$-meson," *The London, Edinburgh, and Dublin Philosophical Magazine and Journal of Science*, vol. 44, no. 357, pp. 1068–1080, 1953.

[18] D. P. Balamuth, R. W. Zurmühle, and S. L. Tabor, "Isospin-forbidden alpha decay of the 15.11-mev state in $^{12}$C," *Phys. Rev. C*, vol. 10, pp. 975–986, Sep 1974.

[19] H. O. U. Fynbo, Y. Prezado, U. C. Bergmann, M. J. G. Borge, P. Dendooven, W. X. Huang, J. Huikari, H. Jeppesen, P. Jones, B. Jonson, M. Meister, G. Nyman, K. Riisager, O. Tengblad, I. S. Vogelius, Y. Wang, L. Weissman, K. W. Rolander, and J. Äystö, "Clarification of the three-body decay of $^{12}$C (12.71 mev)," *Phys. Rev. Lett.*, vol. 91, p. 082502, Aug 2003.

[20] M. Bhattacharya, E. G. Adelberger, and H. E. Swanson, "Precise study of the final-state continua in $^{8}$Li and $^{8}$B decays," *Phys. Rev. C*, vol. 73, p. 055802, May 2006.

[21] K. Siegbahn and E. Hayward, "Alpha-, beta-, and gamma-ray spectroscopy," *Physics Today*, vol. 18, pp. 76–76, 10 1965.

[22] M. Morita and R. Morita, "Beta-gamma angular correlations and beta-ray angular distributions," *Progress of Theoretical Physics Supplement*, vol. 37, pp. 458–472, 03 1966.

[23] V. Zelevinsky, *Physics of Atomic Nuclei*, ch. 24, pp. 585–625. John Wiley & Sons, Ltd, 2017.

[24] R. Steffen, "Search for higher-order effects in allowed beta decay," *Physical Review Letters - PHYS REV LETT*, vol. 3, pp. 277–279, 09 1959.

[25] J. Äystö, "Development and applications of the igisol technique," *Nuclear Physics A*, vol. 693, no. 1, pp. 477–494, 2001. Radioactive Nuclear Beams.

[26] J. Ziegler, J. Biersack, and U. Littmark, "Srim," *The Stopping and Range of Ions in Solids*, 1985. cited By 18092.

[27] Aarhus University Subatomic physics group, "Ausalib," Nov 2021. https://git.kern.phys.au.dk/ausa/ausalib/wikis/home.

[28] S. A. et al., "Geant4—a simulation toolkit," *Nuclear Instruments and Methods in Physics Research Section A: Accelerators, Spectrometers, Detectors and Associated Equipment*, vol. 506, no. 3, pp. 250–303, 2003.

[29] S. Lærkegaard Johansen, "A study of the $\beta-$response of silicon detectors and the effects of backscattering in a complex setup using geant4," Master's thesis, Aarhus University, 2021.

[30] O. Tange, "Gnu parallel 20210222 ('angsangsukyi')," Feb. 2020. GNU Parallel is a general parallelizer to run multiple serial command line programs in parallel without changing them.

[31] A. Rytz, "Recommended energy and intensity values of alpha particles from radioactive decay," *Atomic Data and Nuclear Data Tables*, vol. 47, no. 2, pp. 205–239, 1991.

[32] J. von Neumann, "Various techniques used in connection with random digits," in *Monte Carlo Method* (A. S. Householder, G. E. Forsythe, and H. H. Germond, eds.), vol. 12 of *National Bureau of Standards Applied Mathematics Series*, ch. 13, pp. 36–38, Washington, DC: US Government Printing Office, 1951.

[33] O. Behnke, K. Kröninger, G. Schott, and T. Schörner-Sadenius, *Data analysis in high energy physics: a practical guide to statistical methods*. John Wiley & Sons, 2013.